

intermediate synchrotron-peaked BL Lac (IBL: $10^{14} < \nu_{p,syn} < 10^{15}$ Hz) and high synchrotron-peaked BL Lac (HBL: $\nu_{p,syn} > 10^{15}$ Hz) (Abdo et al., 2010).

Mkn421 is an HBL source located at a redshift $z \sim 0.031$. It is among the brightest nearby very-high-energy (VHE) sources in the extragalactic universe. Mkn421 was first detected in γ -rays by the Energetic Gamma Ray Experiment Telescope (EGRET; Lin et al., 1992). It was also the first confirmed TeV blazar observed by Whipple telescope (Punch et al., 1992; Petry et al., 1996). It has been extensively studied using different observatories across the electromagnetic spectrum (Fossati et al., 2008; Shukla et al., 2012; Sinha et al., 2016; Krawczynski et al., 2001). It exhibits flux variability across all energy bands, particularly in X-ray/ γ -ray bands, on timescales ranging from minutes to days, as reported in several studies (see e.g., Wagner and Witzel, 1995; Falomo et al., 2014; Goyal, 2020). The high variability indicate that the electrons responsible for the emission are highly energetic and have a short cooling time (Aharonian et al., 2007; Ackermann et al., 2016). While number of correlation studies have indicated a zero time lag between X-ray and TeV emissions from Mkn 421 in different flux states (see e.g., Amenomori et al., 2003; Rebillot et al., 2006; Aleksić et al., 2015; Baloković et al., 2016; Arbet-Engels et al., 2021), it is noteworthy that a time lag of 2.1 ± 0.7 ks was observed between X-ray and TeV emissions during the 2001 flaring of Mkn 421 (Fossati et al., 2008). Additionally, investigations focusing on the correlation between optical and X-ray/TeV emissions, such as (Macomb et al., 1995; Cao and Wang, 2013), have reported no significant correlation. These findings lend support to hadronic models and two-zone SSC models.

Observations of Mkn421 in both flaring and quiescent states have revealed a curvature in its X-ray spectrum, with the log parabola model providing the best fit (Goswami et al., 2018; Massaro et al., 2004; Tramacere et al., 2007). In addition to the log-parabola model, different physical models have also been used to reproduce the curvature in the X-ray spectrum in various studies (Goswami et al., 2020; Khatoon et al., 2022; Hota et al., 2021). These studies constrain the physical models by studying the correlation among the model parameters. For example, Hota et al. (2021) demonstrated that it is possible to differentiate between spectrally degenerate models by correlating the spectral parameters. Additionally, with the help of correlation studies one can gain insight into the acceleration mechanism taking place in these systems. Following the same approach, Khatoon et al. (2022) extended the correlation study among model parameters to long term light curve of Mkn 421, and discovered that their results are consistent with the short-term evolution of the source. Apart from these studies, Markowitz et al. (2022) conducted a detailed spectral study of Mkn 421 during January 2019 flaring period. Their findings demonstrated that the broad X-ray spec-

trum could be effectively modeled using a broken power-law model, both in time-averaged and time-resolved scenarios.

Blazar variability has been extensively studied using various theoretical models. Among these, two-zone models have gained significant attention for their ability to explain both steady-state and flaring emissions. Kirk et al. (1998) introduced a framework where particle acceleration occurs near the shock front, while radiation is emitted in a downstream region. This separation highlights the interplay between acceleration and radiative processes, providing critical insights into the multi-wavelength behavior of blazars like Mkn 421. Dmytriiev et al. (2021) analyzed the February 2010 flare of Mrk 421 using a two-zone model, consisting of a steady-state emitting zone responsible for quiescent emission and a transient acceleration zone for flaring activity. Their model predicts the harder-when-brighter trend in soft X-rays as a result of particle acceleration processes, highlighting the dynamic interplay between acceleration and cooling mechanisms. Time-dependent models incorporating particle transport and acceleration mechanisms provide deeper insights into the formation of X-ray spectra and time lags in blazars. Lewis et al. (2016) developed a physical framework using transport equations that account for stochastic acceleration, synchrotron losses, and shock acceleration. Applying this model to Mrk 421, they reproduced both the observed X-ray spectra and time lags, providing important constraints on the physical processes operating in the jet. Kapanadze et al. (2018) analyzed the spectral and flux variability of Mrk 421 during selected epochs, identifying correlations consistent with first- and second-order Fermi acceleration. Their findings emphasize the influence of turbulence and magnetic field variations in shaping the observed X-ray behavior, offering valuable insights into the underlying particle acceleration mechanisms.

Shah et al. (2021) conducted a detailed time resolved X-ray spectral study of HBL 1ES 1959+650. The authors showed that synchrotron emission of a broken power-law electron distribution provided a better fit to the X-ray spectrum than the synchrotron emission of log-parabola model. Further, the authors reported an anticorrelation between the the normalized particle density with the index below the break energy. However, when introducing a delay of approximately 60 ks, a strong positive correlation between the particle density and index was observed. The modelling of such time delays is used to constrain the physical parameters responsible for emission. The investigation of short-term variability properties in jet of Mkn 421 can offer insight into their particle acceleration and emission mechanism. Our study presents an X-ray analysis of Mkn 421 using AstroSat observations taken at various epochs from 2016 to 2019. Following a methodology similar to Shah et al. (2021), we perform a time-resolved spectral analysis to establish correlations between spectral parameters and gain insight into the

system’s nature. The paper is organized as follows: Section 1 covers data reduction, Section 2 presents the results of time variability, time-resolved spectral analysis, and a detailed correlation study. Section 3 offers a summary of our work, followed by an in-depth discussion.

1. DATA REDUCTION

AstroSat telescope, as India’s first multiwavelength observatory, has the unique capability of observing from optical/UV to soft-hard X-ray ranges simultaneously (Agrawal, 2017). It comprises of five payloads, including the Ultra-Violet Imaging Telescope (UVIT) which observes in the 130-300 nm range (Tandon et al., 2017a,b), the Soft X-ray focusing Telescope (SXT) which observes in the 0.3-8.0 keV range (Singh et al., 2016, 2017), the Large Area X-ray Proportional Counter (LAXPC) which observes in the 3-80 keV range (Yadav et al., 2016), and the Cadmium Zinc Telluride Imager (CZTI) which observes in the 10-100 keV range (Rao et al., 2017). During the period 2016-2019, Mkn 421 was observed by AstroSat at different epochs, the details of the observation time and total exposure time of these observations are provided in Table 1. The data were obtained from the AstroSat data archive ASTROBROWSE. Further details on the data reduction for the SXT and LAXPC observations are described below.

1.1. Soft X-ray Telescope (SXT)

The SXT is an X-ray imaging telescope with a focal length of 2 meters, operating in the 0.3-8.0 keV energy range (Singh et al. (2017)). It uses a e2V CCD-22 as its primary detector, which is located at the common focus of all the mirrors. The telescope has an angular resolution of 2 arcmin and a field of view with a diameter of ~ 40 arcmin.

AstroSat observed Mkn 421 in photon counting (PC) mode during different epochs between 2016-2019. The Level-1 data of the source was processed using SXT pipeline version 1.4b (AS1SXTLevel2-1.4b; release date 2019-01-03). The SXTEVTMERGER tool was utilized to merge the level-2 event files from different orbits. Science products such as light curves, images, and spectra were extracted using XSELECT tool version V2.4m distributed with HEASOFT v. 6.29. A circle with a radius of 16 arcmin centered on the source, which included more than 95 percent of the photon counts, was used to extract light curves and spectra. An off-axis auxiliary response file (ARF) appropriate for the specific source region generated by using the sxtARFModule tool, along with a background spectrum ‘SkyBkg comb EL3p5 Cl Rd16p0 v01.pha’, provided by the SXT POC team, and the response matrix file (RMF) ‘sxt pc mat g0to12.rmf’ were used for spectral analysis. In order to ensure optimal counts per bin, “ftgroup-pha” command was used.

Table 1: Observations of Mkn 421 during the flaring events between 2016 and 2019 using the LAXPC and SXT instruments.

Observation	Observation ID	Instrument	Energy (keV)	Exposure (ks)
S1	G05_201T01_9000000478 (2 June, 2016)	SXT	0.7-7.0	11.00
		LAXPC20	3.0-30.0	27.60
S2	A02_005T01_9000000948 (3-8 Jan, 2017)	SXT	0.7-7.0	98.72
		LAXPC20	3.0-30.0	171.10
S3	T01_218T01_9000001852 (19-20 Jan, 2018)	SXT	0.7-7.0	25.00
		LAXPC20	3.0-30.0	31.00
S4	A05_015T01_9000002650 (10-19 Jan, 2019)	SXT	0.7-7.0	111.94
		LAXPC20	3.0-30.0	150.40
S5	A05_204T01_9000002856 (23-28 April, 2019)	SXT	0.7-7.0	104.90
		LAXPC20	3.0-30.0	146.00

Table 2: The fractional root-mean-square variability of the source from the 100 second binned light curves observed by SXT and LAXPC20 during various time periods.

Observation	Observation ID	Instrument	F_{rms}
S1.	G05_201T01_9000000478 (2 June, 2016)	SXT	0.0644 ± 0.0051
		LAXPC20	0.0764 ± 0.0037
S2	A02_005T01_9000000948 (3-8 Jan, 2017)	SXT	0.2103 ± 0.0051
		LAXPC20	0.3159 ± 0.0056
S3	T01_218T01_9000001852 (19-20 Jan, 2018)	SXT	0.1645 ± 0.0077
		LAXPC20	0.2609 ± 0.0110
S4	A05_015T01_9000002650 (10-19 Jan, 2019)	SXT	0.1206 ± 0.0028
		LAXPC20	0.1409 ± 0.0028
S5	A05_204T01_9000002856 (23-28 April, 2019)	SXT	0.1193 ± 0.0028
		LAXPC20	0.1614 ± 0.0031

1.2. Large Area Proportional Counters (LAXPC)

LAXPC is one of the major payloads onboard AstroSat. It is non-focusing instrument with a large total effective area of ($\sim 6000 \text{ cm}^2$). It consist of three X-ray proportional counter units namely LAXPC10, LAXPC20, and LAXPC30. These counters operate in the energy range of 3-80 keV and have a high time resolution of $10 \mu\text{s}$ (Yadav et al., 2016; Antia et al., 2017; Agrawal et al., 2017; Misra et al., 2017). In our work, we utilized data exclusively from LAXPC20, as LAXPC30 was turned off due to abnormal gain changes in March 2018 (Antia et al., 2017), while the application of standard response files to LAXPC10 was not feasible due to high voltage adjustments that occurred in the spring of 2018.

We processed and analyzed the data using the LAXPCSOFT software (version: LAXPCsoftware22Aug15). First, we created a level-2 event file using the command `laxpc_make_event`, and then generated a good time interval (gti) file using `laxpc_make_stdgti` to remove intervals of South Atlantic Anomaly (SAA) and Earth occultation. We used the gti file to create the source light curve and spectra. Since Mkn 421 is faint source for LAXPC, we utilized the scheme of faint source background algorithm, in order to extract the background spectra and light curves for LAXPC 20. The faint source background algorithm is implemented as a part of LAXPCSOFT (Misra et al., 2021).

We performed background subtraction using the standard `FTool lcmath` command. In this work, we limited the spectral analysis to 3-19 keV since the background dominated the spectra at higher energies.

Table 3: The break energy of the broken power-law model obtained by fitting the time-averaged X-ray spectrum of different observations.

Observation	Observation ID	$\xi_{brk}(\sqrt{keV})$
S1	G05_201T01_9000000478	1.7
S2	A02_005T01_9000000948	1.9
S3	T01_218T01_9000001852	1.8
S4	A05_015T01_9000002650	2.1
S5	A05_204T01_9000002856	2.5

2. ANALYSIS

2.1. Time variability

AstroSat observed Mkn 421 at different times during the time period 2016 to 2019 (MJD: 57398-58601). We generated the X-ray light curves of Mkn 421 in the energy range 0.7-7 keV using the SXT instrument, ignoring spectra below 0.7 keV due to poor quantum efficiency (Singh et al., 2017). The LAXPC20 instrument was also used to extract light curves in the energy range 3.0-30 keV, ignoring spectra above 30 keV due to background noise.

The aim is to conduct a detailed X-ray spectral investigation of Mrk 421 by performing the correlation study among the spectral parameters. Therefore, we limited our analysis to AstroSat observations with a sufficient number of data points. The specific details of the X-ray observation like observation periods, the total time of exposure etc are given in Table 1, different observations in the table are identified as S1, S2, S3, S4 and S5. The SXT and LAXPC light curves corresponding to these observations are shown in Figure 1. We used the FTOOL LCSTATS to check the variability of the X-ray light curves. Using this tool, the fractional root-mean-square (F_{rms}) variability were calculated from the 100 sec binned SXT and LAXPC20 light curves. The values of F_{rms} are mentioned in Table 2. With F_{rms} values ranging from 0.06 to 0.21 in SXT and 0.08 to 0.32 in LAXPC, it is evident that the source exhibits significant variability in X-rays.

2.2. X-ray spectral analysis

We used XSPEC version: 12.12.0 to analyze the X-ray spectra of the source in the energy band $\sim 0.7 - 19$ keV. The SXT spectral data were included from 0.7-7.0 keV, while LAXPC data were included from 3.0-19.0 keV. Background spectrum SkyBkgcomb_EL3p5_CI_Rd16p0_v01.pha' was used to estimate background count rate, while the LAXPC background spectra were generated using the code for the faint source background provided by the LAXPC team. We applied a systematic error of 3% throughout the fitting procedure. We used ftgrouppha command which adjusts the "GROUPING" column within a pha file to achieve the optimal binning of the SXT Spectrum. We grouped the LAXPC spectra at a 5 per cent level to obtain three energy bins per resolution.

The X-ray spectrum of Mkn 421 is attributed to synchrotron emission from non-thermal relativistic electrons.

Therefore, we model the X-ray spectrum by assuming that the emission originates from a spherical region with a radius of R. This emission region is filled with a magnetic field, B, and an isotropic distribution of relativistic electrons, $n(\gamma)$, which experience synchrotron loss. The pitch angle averaged power per unit frequency emitted by single electron can be obtained as (Rybicki and Lightman, 1986)

$$P(\gamma, \nu) = \frac{\sqrt{3}\pi q^3 B}{4mc^2} F\left(\frac{\nu}{\nu_c}\right) \quad (1)$$

where,

$\nu_c = \frac{3\gamma^2 q B}{16mc}$ and $F\left(\frac{\nu}{\nu_c}\right)$ is synchrotron power function defined by (Rybicki and Lightman, 1986)

$$F(x) = x \int_x^\infty K_{5/3}(\psi) d\psi \quad (2)$$

here $K_{5/3}(\psi)$ is the modified Bessel function of order 5/3. The synchrotron emissivity resulting from a relativistic electron distribution $n(\gamma)$ can be obtained by utilizing the equation,

$$J_{syn}(\omega, \alpha) = \frac{1}{4\pi} \int_{\gamma_{min}}^{\gamma_{max}} P(\gamma, \omega, \alpha) n(\gamma) d\gamma \quad (3)$$

If we substitute $\xi = \gamma \sqrt{C}$, with $C = 1.36 \times 10^{-11} \frac{\delta B}{1+z}$, where z represents the redshift of the source and δ represents the jet Doppler factor, the amount of synchrotron flux that the observer receives at energy ϵ can be obtained by using the expression (Begelman et al., 1984)

$$F_{syn}(\epsilon) = \frac{\delta^3(1+z)}{d_L^2} V \mathbb{A} \int_{\xi_{min}}^{\xi_{max}} F\left(\frac{\epsilon}{\xi^2}\right) n(\xi) d\xi \quad (4)$$

Here, $\mathbb{A} = \frac{\sqrt{3}\pi e^3 B}{16m_e c^2 \sqrt{C}}$, V refers to the volume of the emission region and d_L represents the luminosity distance.

Our approach involved numerical solving of Equation 4 and incorporating it into XSPEC as a local convolution model, $synconv \otimes n(\xi)$. This enables modeling of the photon spectrum for any particle energy distribution $n(\xi)$. More precisely, in the convolved XSPEC model, the variable "Energy" is defined as $\xi = \sqrt{C}\gamma$. We considered three models for $n(\xi)$, namely the broken power-law (BPL), log-parabola (LP), and power-law with maximum electron energy ($\xi - max$) model for the analysis. The joint spectra from SXT and LAXPC 20 instruments were fitted with the $constant \times TBabs \times Synconv \otimes n(\xi)$. The value for the neutral hydrogen column density (N_H), determined from the LAB survey (Kalberla et al. (2005)), remained fixed at $1.33 \times 10^{20} cm^{-2}$ throughout the fitting procedure. The Galactic absorption is taken into account via the XSPEC TBabs routine. To account for potential variations in the effective areas of the SXT and LAXPC units, a scaling factor was introduced to the SXT spectra. In all spectral fits, the 'gain' command was

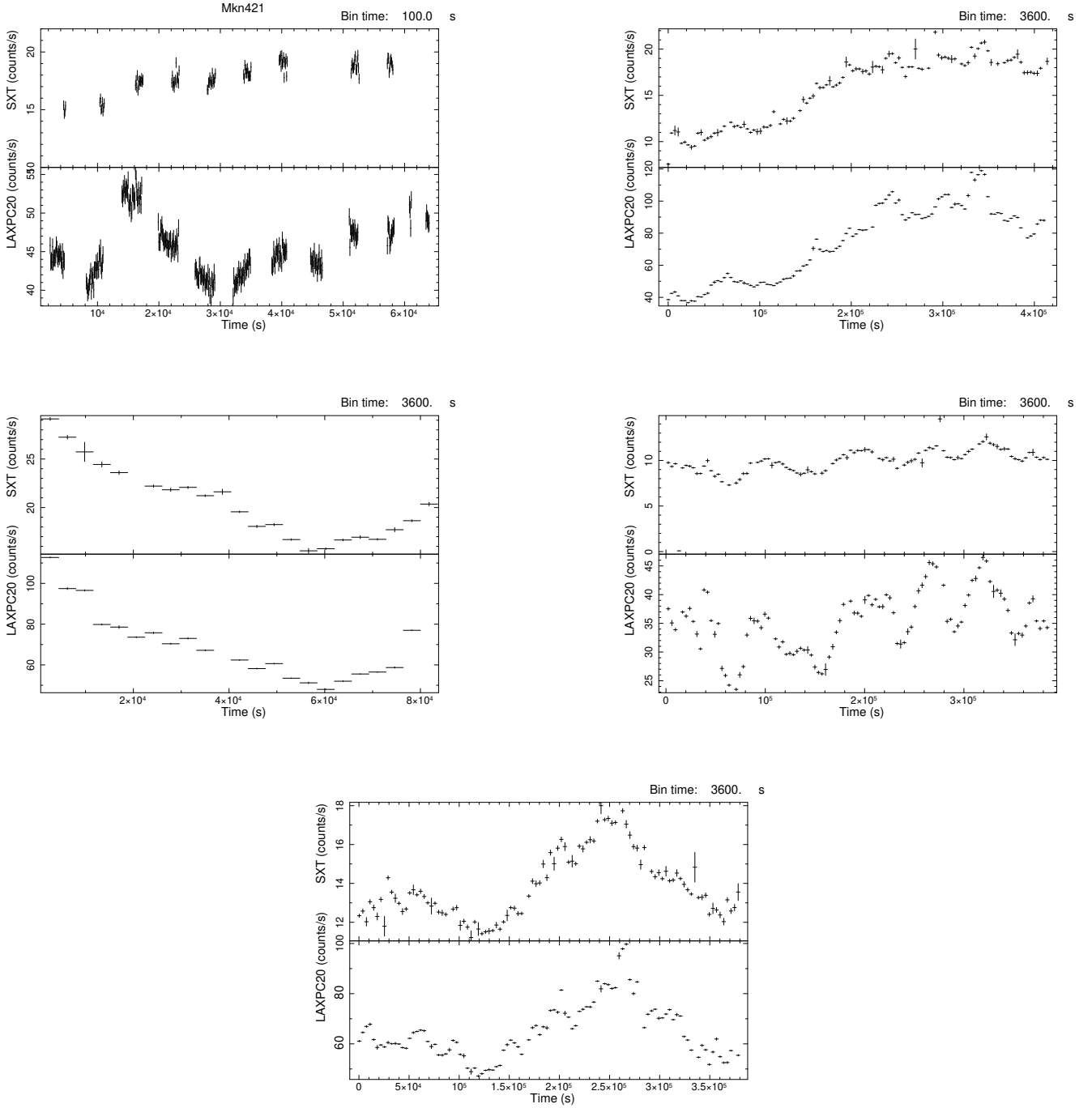


Figure 1: One-hour binned SXT and LAXPC light curves of Mkn 421 obtained in the energy ranges 0.7-7 keV and 3-30 keV, respectively. Each panel corresponds to an individual observation. The upper left and right panels correspond to the S1 and S2 observations, respectively. The middle left and right panels correspond to the S3 and S4 observations, respectively, and the bottom panel corresponds to the S5 observation.

employed, with the gain slope fixed at 1, and the offset allowed to vary. All these models provide a satisfactory fit to the combined SXT and LAXPC spectra. Given the source's high variability in both soft and hard X-ray bands, we investigated the temporal evolution of its X-ray spectral properties. To achieve this, we employed time-resolved spectral analysis by segmenting the total observation period into 10 ks intervals, creating SXT and LAXPC 20 spectra for each segment. In this analysis, we exclusively utilized SXT and LAXPC 20 spectra due to the greater stability of the LAXPC 20 background compared to LAXPC 10. The subsequent section provides a detailed description of these models and their corresponding results.

2.2.1. Broken power-law model

We consider the Broken power-law model (BPL) distribution of electrons and fitted the combined SXT and LAXPC spectra (0.7-19 keV) with $constant \times TBabs \times Synconv \otimes n(\xi)$, here $n(\xi)$ is the BPL distribution, which is given by

$$n(\xi) = K \times \begin{cases} \left(\frac{\xi}{\xi_{ref}}\right)^{-\Gamma_1}, & \xi_{min} < \xi < \xi_{brk} \\ \left(\frac{\xi_{brk}}{\xi_{ref}}\right)^{\Gamma_2-\Gamma_1} \left(\frac{\xi}{\xi_{ref}}\right)^{-\Gamma_2}, & \xi_{brk} < \xi < \xi_{max}, \end{cases} \quad (5)$$

where Γ_1 and Γ_2 represent the indices before and after break energy ξ_{brk} , respectively, K is the normalization of the particle density at the reference energy ξ_{ref} . In the time resolved spectra analysis, we fixed the break energy (ξ_{break}) at the values given in Table 3, which were determined during the fitting of the time-averaged spectrum. We allowed the three parameters - namely, Γ_1 , Γ_2 , and the normalization factor to vary freely. The normalization of the broken power-law model is defined in such a way that it equals the particle density at the break energy. However, this choice is flexible, and the model can be redefined to have the normalization equal to the density at any selected particle energy ξ . In the case of longest duration observation (S4), we calculated the normalization and its associated error for various ξ values of time averaged spectrum. We observed that for $\xi = 1.25 \sqrt{keV}$, the error on the normalization was minimum. Therefore, we adopted this value as the ξ_{ref} for all the observations. It's worth noting that this energy is lower than the break energy for all observations (see Table 3). Therefore, we investigated the correlation between the variation in the lower energy index ($\Delta\Gamma_1$; deviation of Γ_1 from their means) and the variation in the normalized particle density $\frac{\Delta n}{\langle n \rangle}$ (where $\langle n \rangle$ is the mean value of n) at the reference energy (ξ_{ref}). The resulting spectral parameters, along with their respective reduced- χ^2 values, are presented in Table 6,7,8,9 and 10 in the appendix section.

Spearman rank correlation between $\frac{\Delta n}{\langle n \rangle}$ and $\Delta\Gamma_1$ for all observations are given in Table 4. In all observations except S1, a negative correlation between normal-

ized particle density variation and index variation is evident. However, for the S1 observation, we cannot reject the null hypothesis that particle density variation and index variation are uncorrelated (refer to the P_s value in Table 4). As a result, we have chosen not to include the S1 observation data in our subsequent analysis involving the BPL model.

Due to the fact that flux is defined as a function of the normalization and index, it can be inferred that anticorrelation is observed between flux and index (Shah et al. (2021)). This pattern of hardening when brightening is a phenomenon that has been observed in blazars before. We noted that there is no time delay between the normalized particle density variation and the index variation in all of the observations, which is shown in the discrete correlation function (DCF) plots (see Figure 9 in appendix section). The plots in the Figure 2 emphasize that the magnitude of the particle density variation, $|\frac{\Delta n}{\langle n \rangle}|$ and variation in the index $|\Delta\Gamma_1|$ for individual observations as well as for the combined observation are comparable. The amplitude of $\Delta\Gamma$ can exceed that of $\Delta n/n$, when the variation timescale is comparable to the acceleration timescale (τ_{acc}), but in that case the presence of a time lag between the variations in $\Delta n/n$ and $\Delta\Gamma$ is expected (Shah et al., 2021).

BPL at some reference energy, ξ_{ref} and pivot energy, ξ_{piv} before the break energy can be written as,

$$n_{ref} \left[\frac{\xi}{\xi_{ref}} \right]^{-\Gamma_1} = n_{piv} \left[\frac{\xi}{\xi_{piv}} \right]^{-\Gamma_1}, \quad (6)$$

here, n_{ref} and n_{piv} represents the particle densities at reference energy, ξ_{ref} and pivot energy, ξ_{piv} , respectively. Γ_1 is the index of the particle distribution before the break energy. The pivot energy, ξ_{piv} , is defined as the energy at which the particle density remains invariant during variations in the spectral index. This implies that the power-law part of the particle spectrum "rotates" around this point, leading to anti-correlated changes in the particle density and the spectral index. The reference energy, ξ_{ref} , is an arbitrarily chosen energy point used to define the normalization of the particle distribution. In order to obtain the pivot energy and particle density at the pivot energy, Equation 6 can be rearranged such that index before break energy becomes

$$\Gamma_1 = \frac{\log(n_{piv})}{\log\left[\frac{\xi_{ref}}{\xi_{piv}}\right]} - \frac{1}{\log\left[\frac{\xi_{ref}}{\xi_{piv}}\right]} \log(n_{ref}), \quad (7)$$

The variation in $\log n$ is expressed as $\Delta \log n = \log(n + \Delta n) - \log n$. Assuming $\Delta n \ll n$, the normalized particle density variation becomes

$$\frac{\Delta n}{n} = -\Delta\Gamma_1 \log\left[\frac{\xi_{ref}}{\xi_{piv}}\right] \quad (8)$$

Table 4: Spearman correlation results between $\Delta\Gamma_1$ and $\Delta n / \langle n \rangle$ obtained by fitting the synchrotron convolved BPL model to the joint SXT and LAXPC spectra of the selected observations .

Observation	Observation ID	r_s	P_s
S1	G05_201T01_9000000478	-0.41	0.24
S2	A02_005T01_9000000948	-0.95	3.09×10^{-20}
S3	T01_218T01_9000001852	-0.92	5.06×10^{-04}
S4	A05_015T01_9000002650	-0.67	4.7×10^{-06}
S5	A05_204T01_9000002856	-0.65	4.3×10^{-05}

Equation 8 represents a linear equation, with its slope $\log \left[\frac{\xi_{ref}}{\xi_{piv}} \right]$. This slope gives the pivot energy ξ_{piv} with the known ξ_{ref} . We conducted linear fits to the variations of the index $\Delta\Gamma_1$ and the normalized particle density variation $\Delta n / \langle n \rangle$ for each individual observation and for the combined observation (see Figure 2). The ξ_{piv} values resulting from the linear fits in case of broken powerlaw model for observations S2, S3, S4 and S5 are $0.36 \pm 0.04 \sqrt{keV}$, $0.34 \pm 0.06 \sqrt{keV}$, $0.32 \pm 0.08 \sqrt{keV}$ and $0.26 \pm 0.09 \sqrt{keV}$, respectively.

We noted that the pivot energy ξ_{piv} remains same $\xi_{piv} = 0.34 \pm 0.02 \sqrt{keV}$ for the individual observations and also matches with ξ_{piv} obtained for the combined observation ($\xi_{piv,comb} = 0.35 \pm 0.02 \sqrt{keV}$) (see Figure 2). The intercept of Equation 7 can be used to obtain n_{piv} . Therefore, we performed linear fits to the variations in Γ_1 and $\log n$ for individual observations as well as for combined observation (see Figure 3). The obtained values of $\log n_{piv}$ for the individual observations are shown in Figure 3.

To assess the model independence of the same pivot energy in different observations, we employed two models, the log-parabola model and the power-law distribution with maximum electron energy (ξ -max model). Both of these models provided a good fit to the data. Detailed descriptions of these models, along with the observations, are provided below.

2.2.2. Log-parabola model

Previous studies on Mrk421 has showed that the log-parabola model provides a satisfactory statistical fit to the X-ray spectrum (Khatoon et al., 2022; Hota et al., 2021) . Therefore, we fitted the combined X-ray spectra from SXT and LAXPC20 instruments using $constant \times TBabs \times Synconv \otimes n(\xi)$ where $n(\xi)$ is given by a log-parabola form i.e.

$$n(\xi) = K \left(\frac{\xi}{\xi_{ref}} \right)^{-\alpha - \beta \log \left(\frac{\xi}{\xi_{ref}} \right)}, \quad (9)$$

here, α is the particle spectral index at the reference energy, ξ_{ref} , β is the curvature parameter, and K is the normalization of the particle density at $\xi = \xi_{ref}$. While performing the spectral fit in each time bin, we have fixed the ξ_{ref} at 1 keV for all the observations and parameters

α , β , and the normalization were kept free. The model provides a satisfactory fit to the X-ray spectrum, and the resulting spectral parameters, along with their respective reduced- χ^2 values, are presented in Table 6,7,8,9 and 10 in the appendix section.

Table 5 present Spearman correlation results for the log-parabola model fit parameters i.e. between $\Delta\alpha$ and $\Delta\beta$ and between $\Delta\alpha$ and $\Delta n / \langle n \rangle$. Similar to the broken power-law model, all observations except S1, exhibit a negative correlation between $\Delta\alpha$ and the $\Delta n / \langle n \rangle$, indicating a harder spectra when the source is brighter. Additionally, for all observations, a negative correlation is evident between $\Delta\alpha$ and the $\Delta\beta$. No significant correlation was observed in S1 observation. Also, we constructed combined plots of all the observations between $\Delta\alpha$ and the $\Delta n / \langle n \rangle$; and between $\Delta\alpha$ and the $\Delta\beta$ (see Figure 7 in appendix section). These results show the similar correlation trend and thus reproduce the outcomes observed in individual observations.

Moreover, in order to obtain the pivot energy and particle density at pivot energy in LP model, Equation 9 can be written as

$$n_{ref} \left(\frac{\xi}{\xi_{ref}} \right)^{-\alpha - \beta \log \left(\frac{\xi}{\xi_{ref}} \right)} = n_{piv} \left(\frac{\xi}{\xi_{piv}} \right)^{-\alpha' - \beta \log \left(\frac{\xi}{\xi_{piv}} \right)}, \quad (10)$$

here, n_{ref} and n_{piv} represents the particle densities at reference energy, ξ_{ref} and pivot energy, ξ_{piv} , respectively. Following the definition of power law model, the index I , of LP model can be obtained as:

$$I = \alpha + 2\beta \log \left(\frac{\xi}{\xi_{ref}} \right) \quad (11)$$

Matching the indices in equation(10), we get

$$\alpha' = \alpha + 2\beta \log \left(\frac{\xi_{piv}}{\xi_{ref}} \right) \quad (12)$$

Using α' from equation(12) in equation(10),

$$\begin{aligned} \log(n_{ref}) - \left[\alpha + \beta \log \left(\frac{\xi}{\xi_{ref}} \right) \right] \log \left(\frac{\xi}{\xi_{ref}} \right) &= \log(n_{piv}) \\ - \left[\alpha + 2\beta \log \left(\frac{\xi_{piv}}{\xi_{ref}} \right) + \beta \log \left(\frac{\xi}{\xi_{ref}} \right) \right] \log \left(\frac{\xi}{\xi_{piv}} \right) & \end{aligned} \quad (13)$$

$$\log(n_{ref}) - \alpha \log \left(\frac{\xi_{piv}}{\xi_{ref}} \right) = \log(n_{piv}) + \beta \left[\log \left(\frac{\xi_{piv}}{\xi_{ref}} \right) \right]^2 \quad (14)$$

The variation in particle density, α and β would be related through the equation

$$\frac{\Delta n}{n} - \Delta\alpha \log \left(\frac{\xi_{piv}}{\xi_{ref}} \right) = \Delta\beta \left[\log \left(\frac{\xi_{piv}}{\xi_{ref}} \right) \right]^2 \quad (15)$$

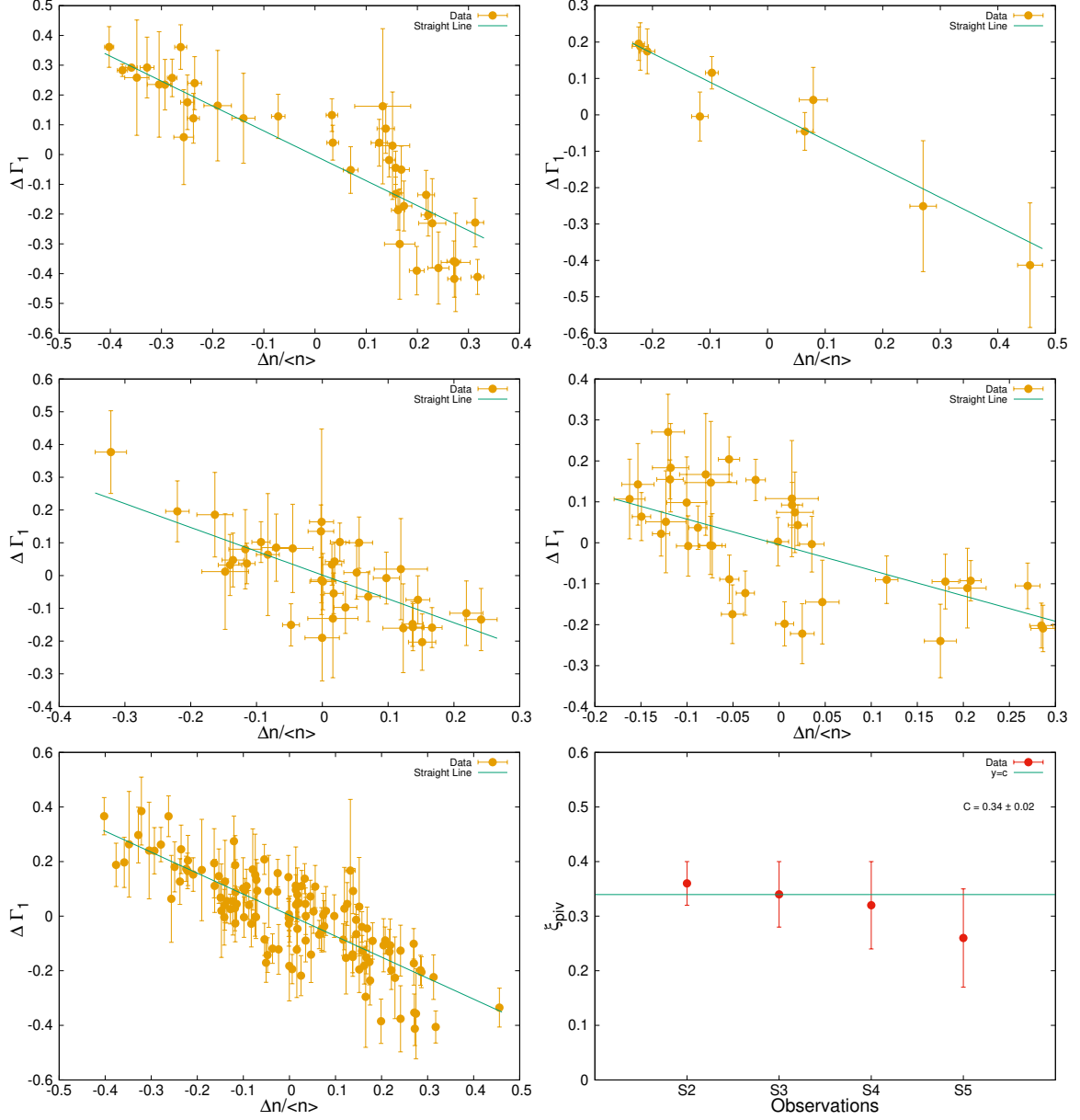


Figure 2: Linear fit to the variations between the spectral index ($\Delta\Gamma_1$) and the normalized particle density ($\Delta n/\langle n \rangle$) at $\xi = \xi_{ref}$ in the BPL model. The upper left and right panels corresponds to S2 and S3 observations respectively, middle left and right panels corresponds to S4 and S5 observations respectively. Bottom left panel represents linear fit for the combined observations. The bottom right plot represents the variation of ξ_{piv} with respect to the observations in the BPL model. The constant fit results in reduced- $\chi^2 \sim 1$ and $\xi_{piv} \sim 0.34 \pm 0.02$ (\sqrt{keV}).

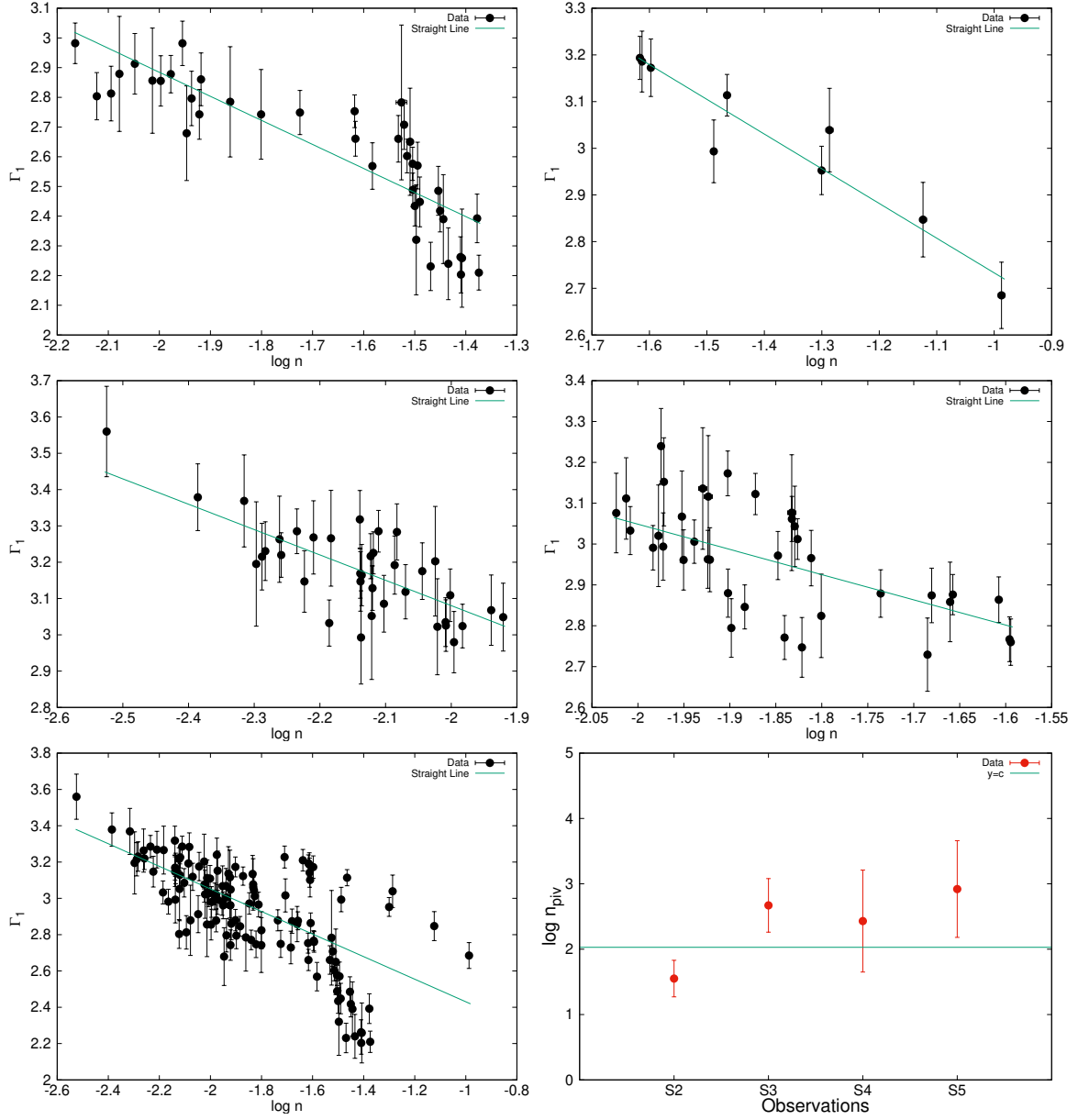


Figure 3: Linear fit to the variations between $\Delta\Gamma_1$ and $\log n$ at $\xi = \xi_{ref}$ in the BPL model. The upper left and right panels corresponds to S2 and S3 observations respectively, middle left and right panels corresponds to S4 and S5 observations respectively. Bottom left panel represents linear fit for the combined observations. The right bottom panel represents the changes in $\log \eta_{piv}$ across all observations in the BPL model.

This equation can be reformulated as:

$$f(x, y) = \frac{1}{t^2}x - \frac{1}{t}y, \quad (16)$$

where, x is $\frac{\Delta n}{n}$, y is $\Delta\alpha$, $f(x, y)$ is $\Delta\beta$ and $t = \log\left(\frac{\xi_{piv}}{\xi_{ref}}\right)$. Clearly the equation 16 is quadratic in t and hence one expects two values of t . We fitted the above equation to the $\frac{\Delta n}{n}$, $\Delta\alpha$, and $\Delta\beta$ values. The fit resulted in two values (positive and negative values) of t . However, we noted that the positive values of t leads to high pivot energy across all observations, contradicting with the observations where pivot energy is often chosen close to the low energy of the observed data. In Figure 4, we have shown the scatter plot for the values of $\frac{\Delta n}{n}$, $\Delta\alpha$, and $\Delta\beta$ along with the fit for the negative roots of t . Upon considering the negative roots, the ξ_{piv} values resulting from the LP model for observations S2, S3, S4, and S5 are $0.57 \pm 0.02 \sqrt{keV}$, $0.53 \pm 0.05 \sqrt{keV}$, $0.58 \pm 0.03 \sqrt{keV}$, and $0.51 \pm 0.07 \sqrt{keV}$, respectively. Consequently, the ξ_{piv} value remains consistent across individual observations, the constant fit resulted in value of $0.56 \pm 0.01 \sqrt{keV}$ (see Figure 4). This value aligns with the ξ_{piv} obtained from combined observations, ($\xi_{piv,comb} = 0.56 \pm 0.02 \sqrt{keV}$).

2.2.3. Power-law distributions with maximum electron energy ($\xi - max$)

We also conducted the broadband X-ray spectral analysis of Mkn 421 by considering the power-law distribution with maximum electron energy. Such particle distribution results in regions in which shock-induced particle acceleration leads to radiative energy loss. The loss becomes dominant at higher energies as the energy loss rate is proportional to the square of its energy. The form of such particle energy distribution can be written as (after transforming γ to $\xi = \sqrt{C}\gamma$)

$$n(\xi) = K \left(\frac{\xi}{\xi_{ref}}\right)^{-p} \left(1 - \frac{\xi}{\xi_{max}}\right)^{(p-2)} \quad (17)$$

where K is particle normalisation, p is the particle spectral index and ξ_{max} corresponds to the maximum Lorentz factor achievable by an electron before energy dissipation occurs. Again the combined X-ray spectrum (0.7-19 keV) in each time bin is jointly fitted with the model $constant \times TBabs \times Synconv \otimes n(\xi)$. During the fitting, we set ξ_{ref} to a fixed value of 1 keV and parameters p , ξ_{max} , and the normalization were kept free. The model provides a satisfactory fit to the X-ray spectrum, and the resulting spectral parameters, along with their respective reduced- χ^2 values, are presented in Table 6,7,8,9 and 10 in the appendix section.

The Spearman correlation results between between Δp and $\Delta n / < n >$, and between Δp and $\Delta\xi_{max}$ are shown in Table 5. No significant correlation was observation S1. A moderate anticorrelation is obtained between Δp and

$\Delta n / < n >$ and a strong positive correlation is observed between $\Delta\xi_{max}$ and Δp . These results are similar to the combined observation plots (see Figure 8 in appendix section). Further like the BPL model, the $\xi - max$ model also shows that the magnitude of index variation are similar to the normalized particle density relation (see Figure 5).

In order to obtain the pivot energy and the particle density at the pivot energy, we can write Equation 17 in the form

$$n_{ref} \left(\frac{\xi}{\xi_{ref}}\right)^{-p} = n_{piv} \left(\frac{\xi}{\xi_{piv}}\right)^{-p} \quad (18)$$

Here, n_{ref} and n_{piv} represents the particle densities at reference energy, ξ_{ref} and pivot energy, ξ_{piv} , respectively. The variation in normalised particle density and p would be related through the equation,

$$\frac{\Delta n}{n} = -\Delta p \log \left[\frac{\xi_{ref}}{\xi_{piv}} \right] \quad (19)$$

This is an equation of a straight line whose slope is given by $\log\left(\frac{\xi_{ref}}{\xi_{piv}}\right)$.

The linear fits are carried to the variations of the index Δp and the normalized particle density variation $\frac{\Delta(n)}{n}$ for the individual observation and for the combined observation (see Figure 5). The ξ_{piv} values resulting from the linear fits in case of $\xi - max$ for observations S2,S3,S4 and S5 are $0.24 \pm 0.06 \sqrt{keV}$, $0.23 \pm 0.05 \sqrt{keV}$, $0.21 \pm 0.06 \sqrt{keV}$ and $0.11 \pm 0.06 \sqrt{keV}$, respectively. We noted that the pivot energy ξ_{piv} remains same ($\xi_{piv} = 0.20 \pm 0.02 \sqrt{keV}$) for the individual observations and also matches with ξ_{piv} obtained for the combined observation (see Figure 5). These results are consistent with those derived from the BPL model, reinforcing the result to be model independent.

3. SUMMARY AND DISCUSSION

We conducted a detailed X-ray spectral analysis of Mkn 421, utilizing data obtained from AstroSat observations spanning multiple epochs from 2016 to 2019. To gain insight into the spectral characteristics on shorter timescales, we employed a time-resolved spectral analysis approach. For this purpose, we divided the total duration of observation for each individual observation into time intervals of 10 ks. In each of these time bins, we observed that the BPL model for particle distribution provided a good fit statistic to the X-ray spectra in the energy range 0.7-19 keV. The lower-energy particle index Γ_1 was observed to exhibit an anticorrelation with the particle density. Furthermore, we found that the variation in the normalized particle density $\frac{\Delta n}{< n >}$ is similar to the variation in the index $\Delta\Gamma_1$. Notably, no time lag was detected between particle density and index. In Shah et al. (2021), the variability in the spectral index (Γ) and particle

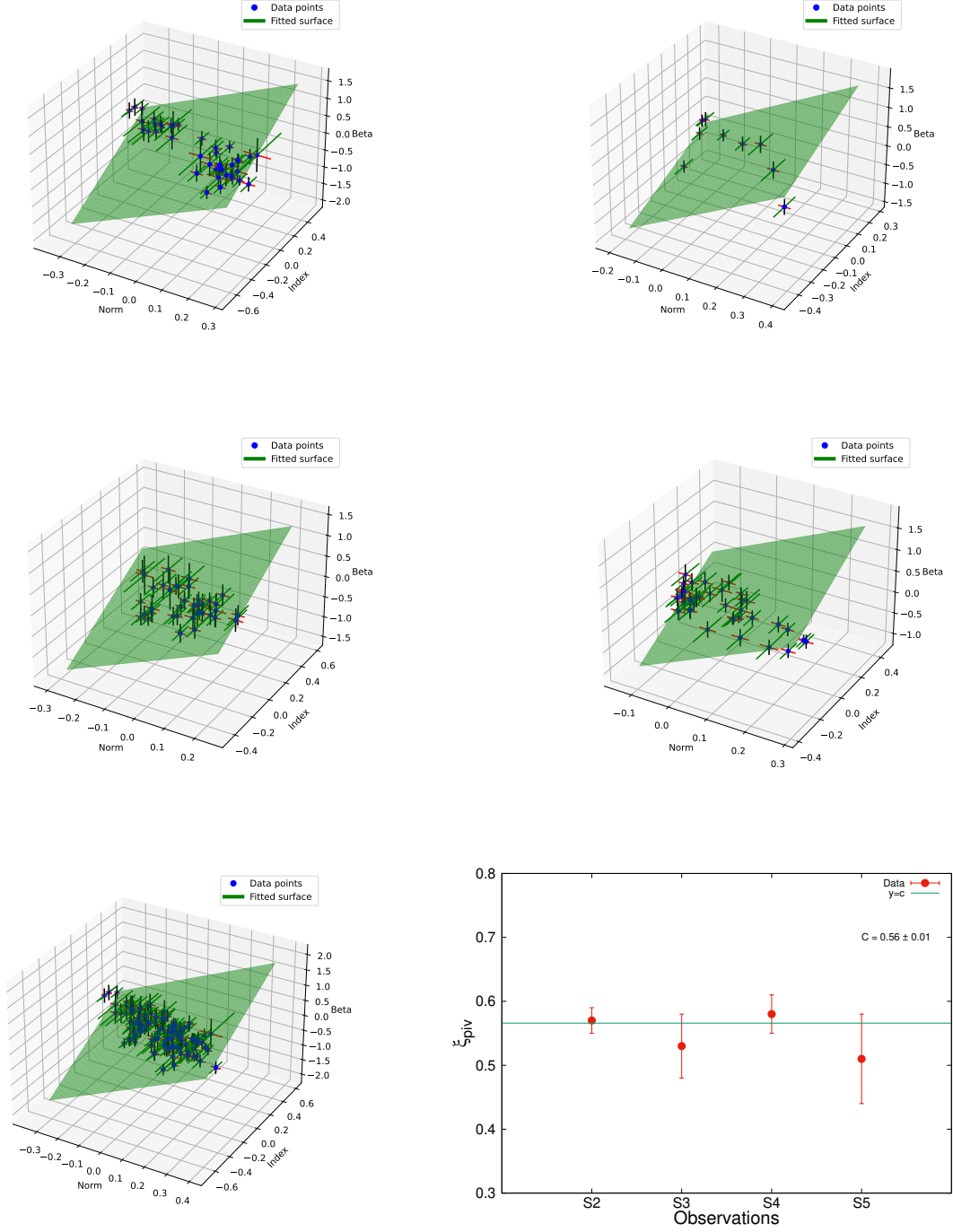


Figure 4: Equation 16 to the variations between the spectral index ($\Delta\Gamma_1$), ($\Delta\beta$) and the normalized particle density ($\Delta n / \langle n \rangle$) at $\xi = \xi_{ref}$ in the LP model. The upper left and right panels corresponds to S2 and S3 observations respectively, middle left and right panels corresponds to S4 and S5 observations respectively. Bottom left panel represents fit for the combined observations. The bottom right plot represents the variation of ξ_{piv} with respect to the observations in the LP model. The constant fit results in reduced- $\chi^2 \sim 1$ and $\xi_{piv} \sim 0.56 \pm 0.01$ (\sqrt{keV}).

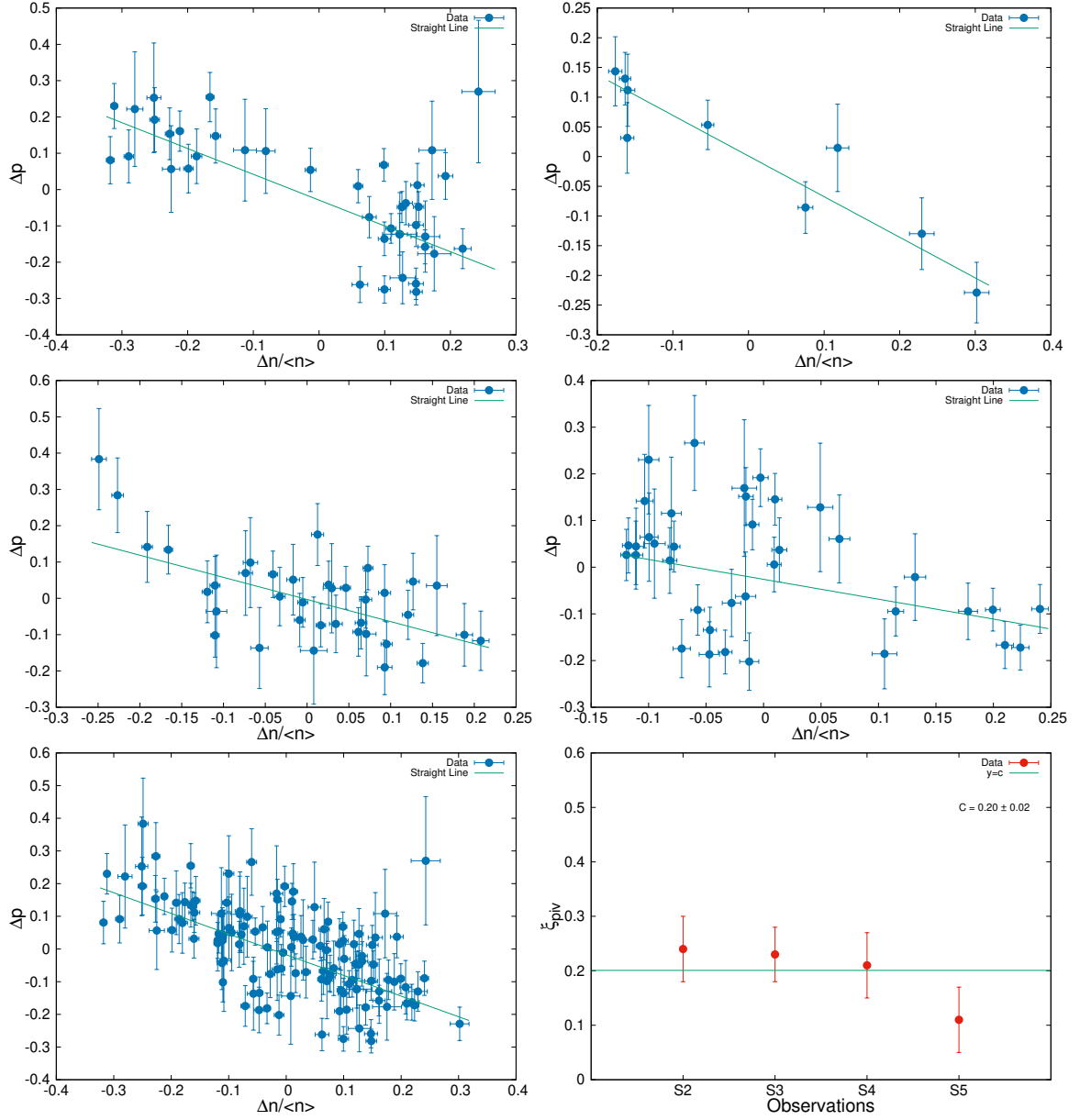


Figure 5: Linear fit to the variations between the spectral index (Δp) and the normalized particle density ($\Delta n / \langle n \rangle$) at $\zeta = \zeta_{ref}$ in the $\zeta - max$ model. The upper left and right panels corresponds to S2 and S3 observations respectively, middle left and right panels corresponds to S4 and S5 observations respectively. Bottom left panel represents linear fit for the combined observations. The bottom right plot represents the variation of ζ_{piv} with respect to the observations in the $\zeta - max$ model. The constant fit results in reduced- $\chi^2 \sim 1$ and $\zeta_{piv} \sim 0.20 \pm 0.02$ (\sqrt{keV}).

Table 5: Spearman correlation results between the best fit spectral parameters obtained by fitting the joint SXT and LAXPC spectra with the synchrotron convolved LP and $\zeta - max$ models.

Observation	Observation ID	Model	Correlation between	r_s	P_s	Correlation between	r_s	P_s
S1.	G05_201T01_9000000478			-0.08	0.87		0.08	0.87
S2	A02_005T01_9000000948	Log-parabola	$\Delta\alpha$ & $\frac{\Delta n}{\langle n \rangle}$	-0.83	4.71×10^{-11}	$\Delta\alpha$ & $\Delta\beta$	-0.70	6.10×10^{-07}
S3	T01_218T01_9000001852			-0.86	2.49×10^{-03}		-0.65	0.05
S4	A05_015T01_9000002650			-0.63	2.31×10^{-05}		-0.63	3.03×10^{-05}
S5	A05_204T01_9000002856			-0.51	0.005		-0.73	3.31×10^{-07}
S No.	Observation ID			Model	Correlation between		r_s	P_s
S1.	G05_201T01_9000000478			-0.37	0.46		0.31	0.54
1.	A02_005T01_9000000948	$\zeta - max$	Δp & $\frac{\Delta n}{\langle n \rangle}$	-0.57	0.12×10^{-04}	Δp & $\Delta\zeta_{max}$	0.73	1.03×10^{-07}
2.	T01_218T01_9000001852			-0.93	2.35×10^{-04}		0.77	0.015
3.	A05_015T01_9000002650			-0.50	0.15×10^{-03}		0.64	2.00×10^{-05}
4.	A05_204T01_9000002856			-0.33	0.042		0.78	7.06×10^{-09}

density is modeled as arising from variations in the acceleration timescale (τ_{acc}). A sinusoidal perturbation in τ_{acc} leads to correlated variations in $\Delta n/n$ and $\Delta\Gamma$, but the relationship between their amplitudes and the presence of a time lag depends on the relative timescales of the system. When the variation timescale is comparable to τ_{acc} , the amplitude of $\Delta\Gamma$ can significantly exceed that of $\Delta n/n$. In this scenario, a notable time lag between the variations in $\Delta n/n$ and $\Delta\Gamma$ is expected, as described by Equation (14) in Shah et al. (2021), which is not observed in our results. However, for slow variations, the phase lag term $(\phi_{\text{lag}}/\sin(\phi_{\text{lag}}))$ in Equation (14) approaches unity. This leads to the steady-state solution represented by Equation (8) in Shah et al. (2021), where the amplitudes of $\Delta n/n$ is greater than $\Delta\Gamma$.

Power-law particle distribution pivots over some energy ξ_0 . In case of BPL distribution of electrons, we found $\frac{\Delta n}{\langle n \rangle}$ to be inversely correlated to Γ_1 , which suggest the harder when brighter feature typically observed in blazars. The linear fits applied to the variations of the index Γ_1 and the normalized particle density $\frac{\Delta n}{\langle n \rangle}$ indicate that the pivot energy ξ_{piv} remains consistent ($\xi_{\text{piv}} = 0.34 \pm 0.02 \sqrt{keV}$) across individual observations, and matches with the ξ_{piv} derived from the combined observation. The steady nature of the pivot energy across different observations carries significant implications. Within context of the convolved model, the ξ parameter is defined as $\xi = \sqrt{C}\gamma$. Consequently, any model parameter, such as the pivot energy ξ_{piv} , can be linked to γ_{piv} as $\gamma_{\text{piv}} = \xi_{\text{piv}}/\sqrt{C}$, here, $C = 1.36 \times 10^{-11} \frac{\delta B}{1+z}$. Given that the estimated ξ_{piv} remains constant, the product of $\delta^{1/2}$ and $B^{1/2}$ should also remain constant. Thus we are unable to separate them to constrain either δ or B individually. Moreover, constant ξ_{piv} suggests that the source's variability stems from index variations and is unaffected by normalization. Consequently, factors such as magnetic fields, source region geometry, and other parameters do not contribute to the source's variability. Instead, the variations are primarily linked to the acceleration or escape timescales associated with the emitted particles within the source.

To assess the model independence of the constancy of the pivot energy, we employed two models, the LP model and the ξ -max model. Besides the BPL model, these alternative models also provide equally good fit to the spectrum. The LP model is characterised by the curved features defined by the parameter, β . The conventional explanation for the curvature in the spectrum involves considering the energy-dependent acceleration/escape rates process (Massaro et al., 2004; Hota et al., 2021). The correlation study between the spectral parameters of LP model shows a negative correlation between $\Delta\alpha$ and the $\Delta n/\langle n \rangle$, indicating a harder spectra when the source is brighter. Additionally, for all observations, a negative correlation is evident between $\Delta\alpha$ and the $\Delta\beta$. No signif-

icant correlation was observed in S1 observation. Within the framework of the LP particle distribution, $\log\left(\frac{\xi_{\text{piv}}}{\xi_{\text{ref}}}\right)$ yields two roots, one positive and one negative. The positive root results in a high pivot energy across all observations, which contradicts typical expectations where the pivot energy is often selected close to the low energy of the observed data. The ξ_{piv} values obtained from the negative root for observations S2, S3, S4, and S5 are all consistent with the value $0.56 \pm 0.01 \sqrt{keV}$. This, once again, indicates the constancy of the pivot energy across different observations.

We further examined the broadband X-ray spectral analysis of Mkn421 by considering the power-law distribution with maximum electron energy. Such particle distribution results in regions in which shock-induced particle acceleration leads to radiative energy loss. The loss becomes dominant at higher energies as the energy loss rate is proportional to the square of its energy, leading to a departure from a power-law form at high energies with a maximum Lorentz factor γ_{max} . We observed that each of the spectra can be adequately represented by this model. The index of the particle distribution at lower energies exhibited a positive correlation with the maximum energy of the particles. However, according to a simplistic interpretation where the observed variation primarily arises from changes in the acceleration time-scale, the correlation should have been negative. A more intricate model, in which the magnetic field is correlated with the acceleration time-scale, could account for the positive correlation observed. By examining the relationship between particle densities at different energy scales we established an inverse correlation between $\Delta n/\langle n \rangle$ and Δp , a pattern that aligns with the observed data. Linear fits applied to the variations of the spectral index Δp and the normalized particle density $\Delta n/\langle n \rangle$ for each individual observation, as well as for the combined observation, enables us to estimate the values of ξ_{piv} . Again we noted that ξ_{piv} remains constant ($\xi_{\text{piv}} = 0.20 \pm 0.02(\sqrt{keV})$) for individual observations, and are consistent with the ξ_{piv} obtained for the combined observation. These results are consistent with those obtained from the BPL model, underscoring the model independence of the result. This identification enables us to investigate the underlying causes of variability.

The observed anti-correlation between the electron density and spectral index, along with the constant pivot Lorentz factor, suggests that these variations may be attributed to changes in the acceleration time scales. However, the potential influence of other time scales, such as the escape time scale and injection rates can not be ruled out. In this context, Hota et al. (2021) investigated the X-ray variability of Mrk 421 by incorporating an energy-dependent escape time scale (EDD). Their study showed that while the EDD and EDA models effectively describe the spectra for individual time segments and ex-

plain the correlations among spectral parameters within the model framework, the derived physical parameter estimates challenge the validity of these models in their simplest form. Since the log-parabola model is essentially an approximation of the such model, the similar correlation trends observed between the fitting parameters in their study and ours can be used to challenge the hypothesis of energy-dependent escape/acceleration time scales. Additionally, the constant pivot energy observed across the observations indicate that their is minor feedback of B and δ on the particle spectrum. Moderate changes in δ and B would not affect the constant pivot energy directly, but they may amplify or suppress the observed flux variability. Thus, while external variations cannot be entirely ruled out, the pivot energys stability points toward intrinsic energy-dependent processes as the primary drivers of variability. In conclusion, the models like EDD and EDA are simplified, with analytical solutions, but the actual physical processes are likely more intricate. Developing and implementing advanced methods to test non-analytical models is crucial. For instance, both acceleration and diffusion time-scales may exhibit energy dependence, which would be more physically realistic (Massaro et al., 2004, 2006; Tramacere et al., 2007). Stochastic acceleration might play a significant role in shaping the particle distribution.

4. Acknowledgements

SAD is thankful to the MOMA for the MANF fellowship (No.F.82-27/2019(SA-III)). ZS is supported by the Department of Science and Technology, Govt. of India, under the INSPIRE Faculty grant (DST/INSPIRE/04/2020/002319). SAD, ZS and NI express gratitude to the Inter-University Centre for Astronomy and Astrophysics (IUCAA) in Pune, India, for the support and facilities provided.

References

- Abdo, A., Ackermann, M., Agudo, I., Ajello, M., Aller, H., Aller, M., Angelakis, E., Arkharov, A., Axelsson, M., Bach, U., et al., 2010. The spectral energy distribution of fermi bright blazars. *The Astrophysical Journal* 716, 30.
- Ackermann, M., Anantua, R., Asano, K., Baldini, L., Barbiellini, G., Bastieri, D., Gonzalez, J.B., Bellazzini, R., Bissaldi, E., Blandford, R., et al., 2016. Minute-timescale γ -ray variability during the giant outburst of quasar 3c 279 observed by fermi-lat in 2015 june. *The Astrophysical journal letters* 824, L20.
- Agrawal, P.C., 2017. AstroSat: From Inception to Realization and Launch. *Journal of Astrophysics and Astronomy* 38, 27. doi:10.1007/s12036-017-9449-6.
- Agrawal, P.C., Yadav, J.S., Antia, H.M., Dedhia, D., Shah, P., Chauhan, J.V., Manchanda, R.K., Chitnis, V.R., Gujar, V.M., Katoch, T., Kurhade, V.N., Madhwani, P., Manojkumar, T.K., Nikam, V.A., Pandya, A.S., Parmar, J.V., Pawar, D.M., Roy, J., Paul, B., Pahari, M., Misra, R., Ravichandran, M.H., Anilkumar, K., Joseph, C.C., Navalgund, K.H., Pandiyan, R., Sarma, K.S., Subbarao, K., 2017. Large Area X-Ray Proportional Counter (LAXPC) Instrument on AstroSat and Some Preliminary Results from its Performance in the Orbit. *Journal of Astrophysics and Astronomy* 38, 30. doi:10.1007/s12036-017-9451-z, arXiv:1705.06446.
- Aharonian, F., Akhperjanian, A.G., Bazer-Bachi, A.R., Behera, B., Beilicke, M., Benbow, W., Berge, D., Bernlöhner, K., Boisson, C., Bolz, O., Borrel, V., Boutelier, T., Braun, I., Brion, E., Brown, A.M., Bühler, R., Büsching, I., Bulik, T., Carrigan, S., Chadwick, P.M., Clapson, A.C., Chounet, L.M., Coignet, G., Cornils, R., Costamante, L., Degrange, B., Dickinson, H.J., Djannati-Ataï, A., Domainko, W., Drury, L.O., Dubus, G., Dyks, J., Egberts, K., Emmanoulopoulos, D., Espigat, P., Farnier, C., Feinstein, F., Fiasson, A., Förster, A., Fontaine, G., Funk, S., Funk, S., Füßling, M., Gallant, Y.A., Giebels, B., Glienstein, J.F., Glück, B., Goré, P., Hadjichristidis, C., Hauser, D., Hauser, M., Heinzlmann, G., Henri, G., Hermann, G., Hinton, J.A., Hoffmann, A., Hofmann, W., Holleran, M., Hoppe, S., Horns, D., Jacholkowska, A., de Jager, O.C., Kendziorra, E., Kerschhaggl, M., Khélifi, B., Komin, N., Kosack, K., Lamanna, G., Latham, I.J., Le Gallou, R., Lemièrre, A., Lemoine-Goumard, M., Lenain, J.P., Lohse, T., Martin, J.M., Martineau-Huynh, O., Marcowith, A., Masterson, C., Maurin, G., McComb, T.J.L., Moderski, R., Moulin, E., de Naurois, M., Nedbal, D., Nolan, S.J., Olive, J.P., Orford, K.J., Osborne, J.L., Ostrowski, M., Panter, M., Pedalletti, G., Pelletier, G., Petrucci, P.O., Pita, S., Pühlhofer, G., Punch, M., Ranchon, S., Raubenheimer, B.C., Raue, M., Rayner, S.M., Renaud, M., Ripken, J., Rob, L., Rolland, L., Rosier-Lees, S., Rowell, G., Rudak, B., Ruppel, J., Sahakian, V., Santangelo, A., Saugé, L., Schlenker, S., Schlickeiser, R., Schröder, R., Schwanke, U., Schwarzburg, S., Schwemmer, S., Shalchi, A., Sol, H., Spangler, D., Stawarz, L., Steenkamp, R., Stegmann, C., Superina, G., Tam, P.H., Tavernet, J.P., Terrier, R., van Eldik, C., Vasileiadis, G., Venter, C., Vialle, J.P., Vincent, P., Vivier, M., Völk, H.J., Volpe, F., Wagner, S.J., Ward, M., Zdziarski, A.A., 2007. An Exceptional Very High Energy Gamma-Ray Flare of PKS 2155-304. *The Astrophysical Journal Letters* 664, L71-L74. doi:10.1086/520635, arXiv:0706.0797.
- Aleksić, J., Ansoldi, S., Antonelli, L.A., Antoranz, P., Babic, A., Bangale, P., De Almeida, U.B., Barrio, J., González, J.B., Bednarek, W., et al., 2015. Unprecedented study of the broadband emission of mrk 421 during flaring activity in march 2010. *Astronomy & Astrophysics* 578, A22.
- Amenomori, M., Ayabe, S., Cui, S., Ding, L., Ding, X., Feng, C., Feng, Z., Gao, X., Geng, Q., Guo, H., et al., 2003. Multi-teV gamma-ray flares from markarian 421 in 2000 and 2001 observed with the tibet air shower array. *The Astrophysical Journal* 598, 242.
- Antia, H.M., Yadav, J.S., Agrawal, P.C., Verdhhan Chauhan, J., Manchanda, R.K., Chitnis, V., Paul, B., Dedhia, D., Shah, P., Gujar, V.M., Katoch, T., Kurhade, V.N., Madhwani, P., Manojkumar, T.K., Nikam, V.A., Pandya, A.S., Parmar, J.V., Pawar, D.M., Pahari, M., Misra, R., Navalgund, K.H., Pandiyan, R., Sharma, K.S., Subbarao, K., 2017. Calibration of the Large Area X-Ray Proportional Counter (LAXPC) Instrument on board AstroSat. *Astrophysical Journal Supplement Series* 231, 10. doi:10.3847/1538-4365/aa7a0e, arXiv:1702.08624.
- Arbet-Engels, A., Baack, D., Balbo, M., Biland, A., Blank, M., Bretz, T., Bruegge, K., Bulinski, M., Buss, J., Doerr, M., Dorner, D., Elsaesser, D., Hildebrand, D., Mannheim, K., Mueller, S.A., Neise, D., Noethe, M., Paravac, A., Rhode, W., Schleicher, B., Sedlaczek, K., Shukla, A., Sliusar, V., Walter, R., von Willert, E., 2021. The relentless variability of Mrk 421 from the TeV to the radio. *Astronomy & Astrophysics* 647, A88. doi:10.1051/0004-6361/201935557, arXiv:2101.10651.
- Baloković, M., Paneque, D., Madejski, G., Furniss, A., Chiang, J., Ajello, M., Alexander, D.M., Barret, D., Blandford, R.D., Boggs, S.E., Christensen, F.E., Craig, W.W., Forster, K., Giommi, P., Grefenstette, B., Hailey, C., Harrison, F.A., Hornstrup, A., Kitaguchi, T., Koglin, J.E., Madsen, K.K., Mao, P.H., Miyasaka, H., Mori, K., Perri, M., Pivovarov, M.J., Puccetti, S., Rana, V., Stern, D., Tagliaferri, G., Urry, C.M., Westergaard, N.J., Zhang, W.W., Zoglauer, A., NuSTAR Team, Archambault, S., Archer, A., Barnacka, A., Benbow, W., Bird, R., Buckley, J.H., Bugaev, V., Cerruti, M., Chen, X., Ciupik, L., Connolly, M.P., Cui, W., Dickinson, H.J., Dumm, J., Eisch, J.D., Falcone, A., Feng, Q., Finley, J.P., Fleischhack, H., Fortson, L., Griffin, S., Griffiths, S.T., Grube, J., Gyuk, G., Huettner, M., Hkansson, N., Holder, J., Humen-

- sky, T.B., Johnson, C.A., Kaaret, P., Kertzman, M., Khassen, Y., Kieda, D., Krause, M., Krennrich, F., Lang, M.J., Maier, G., McArthur, S., Meagher, K., Moriarty, P., Nelson, T., Nieto, D., Ong, R.A., Park, N., Pohl, M., Popkow, A., Poeschel, E., Reynolds, P.T., Richards, G.T., Roache, E., Santander, M., Sembroski, G.H., Shahinyan, K., Smith, A.W., Staszak, D., Telezhinsky, I., Todd, N.W., Tucci, J.V., Tyler, J., Vincent, S., Weinstein, A., Wilhelm, A., Williams, D.A., Zitzer, B., VERITAS Collaboration, Ahnen, M.L., Ansoldi, S., Antonelli, L.A., Antoranz, P., Babic, A., Banerjee, B., Bangale, P., Barres de Almeida, U., Barrio, J.A., Becerra González, J., Bednarek, W., Bernardini, E., Bisuzzi, B., Biland, A., Blanch, O., Bonnefoy, S., Bonnoli, G., Borraacci, F., Bretz, T., Carmona, E., Carosi, A., Chatterjee, A., Clavero, R., Colin, P., Colombo, E., Contreras, J.L., Cortina, J., Covino, S., Da Vela, P., Dazzi, F., De Angelis, A., De Lotto, B., de Oña Wilhelmi, E., Delgado Mendez, C., Di Pierro, F., Dominis Prester, D., Dorner, D., Doro, M., Einecke, S., Elsaesser, D., Fernández-Barral, A., Fidalgo, D., Fonseca, M.V., Font, L., Frantzen, K., Fruck, C., Galindo, D., García López, R.J., Garczarczyk, M., Garrido Terrats, D., Gaug, M., Giammaria, P., Glawion (Eisenacher, D., Godinović, N., González Muñoz, A., Guberman, D., Hahn, A., Hanabata, Y., Hayashida, M., Herrera, J., Hose, J., Hrupec, D., Hughes, G., Idec, W., Kodani, K., Konno, Y., Kubo, H., Kushida, J., La Barbera, A., Las, D., Lindfors, E., Lombardi, S., Longo, F., López, M., López-Coto, R., López-Oramas, A., Lorenz, E., Majumdar, P., Makariev, M., Mallot, K., Maneva, G., Manganaro, M., Mannheim, K., Maraschi, L., Marcote, B., Mariotti, M., Martínez, M., Mazin, D., Menzel, U., Miranda, J.M., Mirzoyan, R., Moralejo, A., Moretti, E., Nakajima, D., Neustroev, V., Niedzwiecki, A., Nieves Rosillo, M., Nilsson, K., Nishijima, K., Noda, K., Orito, R., Overkemping, A., Paiano, S., Palacio, J., Palatiello, M., Paoletti, R., Paredes, J.M., Paredes-Fortuny, X., Persic, M., Poutanen, J., Prada Moroni, P.G., Prandini, E., Puljak, I., Rhode, W., Ribó, M., Rico, J., Rodriguez Garcia, J., Saito, T., Satalecka, K., Scapin, V., Schultz, C., Schweizer, T., Shore, S.N., Sillanpää, A., Sitarek, J., Snidaric, I., Sobczynska, D., Stamerra, A., Steinbring, T., Strzys, M., Takalo, L., Takami, H., Tavecchio, F., Temnikov, P., Terzić, T., Tescaro, D., Teshima, M., Thaele, J., Torres, D.F., Toyama, T., Treves, A., Verguillov, V., Vovk, I., Ward, J.E., Will, M., Wu, M.H., Zanin, R., MAGIC Collaboration, Perkins, J., Verrecchia, F., Leto, C., Böttcher, M., Villata, M., Raiteri, C.M., Acosta-Pulido, J.A., Bachev, R., Berdyugin, A., Blinov, D.A., Carnerero, M.I., Chen, W.P., Chinchilla, P., Damjanovic, G., Eswaraiah, C., Grishina, T.S., Ibryamov, S., Jordan, B., Jorstad, S.G., Joshi, M., Kopatskaya, E.N., Kurtanidze, O.M., Kurtanidze, S.O., Larionova, E.G., Larionova, L.V., Larionov, V.M., Latev, G., Lin, H.C., Marscher, A.P., Mokrushina, A.A., Morozova, D.A., Nikolashvili, M.G., Semkov, E., Smith, P.S., Strigachev, A., Troitskaya, Y.V., Troitsky, I.S., Vince, O., Barnes, J., Güver, T., Moody, J.W., Sadun, A.C., Sun, S., Hovatta, T., Richards, J.L., Max-Moerbeck, W., Readhead, A.C.R., Lähteenmäki, A., Tornikoski, M., Tammi, J., Ramakrishnan, V., Reinthal, R., Angelakis, E., Fuhrmann, L., Myserlis, I., Karamanavis, V., Sievers, A., Ungerechts, H., Zensus, J.A., 2016. Multiwavelength Study of Quiescent States of Mrk 421 with Unprecedented Hard X-Ray Coverage Provided by NuSTAR in 2013. *The Astrophysical Journal* 819, 156. doi:10.3847/0004-637X/819/2/156, arXiv:1512.02235.
- Begelman, M.C., Blandford, R.D., Rees, M.J., 1984. Theory of extragalactic radio sources. *Reviews of Modern Physics* 56, 255.
- Bhatta, G., Dhital, N., 2020. The nature of γ -ray variability in blazars. *The Astrophysical Journal* 891, 120.
- Bhatta, G., Ostrowski, M., Markowitz, A., Akitaya, H., Arkharov, A., Bachev, R., Benítez, E., Borman, G., Carosati, D., Cason, A., et al., 2016. Multifrequency photo-polarimetric web observation campaign on the blazar s5 0716+ 714: Source microvariability and search for characteristic timescales. *The Astrophysical Journal* 831, 92.
- Błażejowski, M., Sikora, M., Moderski, R., Madejski, G.M., 2000. Comptonization of Infrared Radiation from Hot Dust by Relativistic Jets in Quasars. *The Astrophysical Journal* 545, 107–116. doi:10.1086/317791, arXiv:astro-ph/0008154.
- Böttcher, M., Marscher, A.P., Ravasio, M., Villata, M., Raiteri, C.M., Aller, H.D., Aller, M.F., Teräsraanta, H., Mang, O., Tagliaferri, G., Aharonian, F., Krawczynski, H., Kurtanidze, O.M., Nikolashvili, M.G., Ibrahimov, M.A., Papadakis, I.E., Tsinganos, K., Sadakane, K., Okada, N., Takalo, L.O., Sillanpää, A., Tosti, G., Ciprini, S., Frasca, A., Marilli, E., Robb, R., Noble, J.C., Jorstad, S.G., Hagen-Thorn, V.A., Larionov, V.M., Nesci, R., Maesano, M., Schwartz, R.D., Basler, J., Gorham, P.W., Iwamatsu, H., Kato, T., Pullen, C., Benítez, E., de Diego, J.A., Moilanen, M., Oksanen, A., Rodriguez, D., Sadun, A.C., Kelly, M., Carini, M.T., Miller, H.R., Catalano, S., Dultzin-Hacyan, D., Fan, J.H., Ghisellini, G., Ishioka, R., Karttunen, H., Keinänen, P., Kudryavtseva, N.A., Lainela, M., Lanteri, L., Larionova, E.G., Matsumoto, K., Mattox, J.R., McHardy, I., Montagni, F., Nucciarelli, G., Ostorero, L., Papamastorakis, J., Pasanen, M., Sobrito, G., Uemura, M., 2003. Coordinated Multiwavelength Observations of BL Lacertae in 2000. *The Astrophysical Journal* 596, 847–859. doi:10.1086/378156, arXiv:astro-ph/0307022.
- Böttcher, M., Reimer, A., Sweeney, K., Prakash, A., 2013. Leptonic and hadronic modeling of fermi-detected blazars. *The Astrophysical Journal* 768, 54.
- Bregman, J., Lebofsky, M., Aller, M., Rieke, G., Aller, H., Hodge, P., Glassgold, A., Huggins, P., 1981. Multifrequency observations of the red qso 1413 + 135. *Nature* 293, 714–717. doi:10.1038/293714a0.
- Cao, G., Wang, J., 2013. Particle acceleration and emission processes in mrk 421. *Publications of the Astronomical Society of Japan* 65, 109–109.
- Dermer, C.D., Schlickeiser, R., Mastichiadis, A., 1992. High-energy gamma radiation from extragalactic radio sources. *Astronomy & Astrophysics* 256, L27–L30.
- Dmytriiev, A., Sol, H., Zech, A., 2021. Connecting steady emission and very high energy flaring states in blazars: the case of Mrk 421. *Monthly Notices of the Royal Astronomical Society* 505, 2712–2730. doi:10.1093/mnras/stab1445, arXiv:2105.12480.
- Falomo, R., Pian, E., Treves, A., 2014. An optical view of bl lacertae objects. *The Astronomy and Astrophysics Review* 22, 1–38.
- Fossati, G., Buckley, J., Bond, I., Bradbury, S., Carter-Lewis, D., Chow, Y., Cui, W., Falcone, A., Finley, J., Gaidos, J., et al., 2008. Multiwavelength observations of markarian 421 in 2001 march: An unprecedented view on the x-ray/tev correlated variability. *The Astrophysical Journal* 677, 906.
- Ghisellini, G., Padovani, P., Celotti, A., Maraschi, L., 1993. Relativistic Bulk Motion in Active Galactic Nuclei. *The Astrophysical Journal* 407, 65. doi:10.1086/172493.
- Ghisellini, G., Villata, M., Raiteri, C., Bosio, S., De Francesco, G., Latini, G., Maesano, M., Massaro, E., Montagni, F., Nesci, R.a., et al., 1997. Optical-iue observations of the gamma-ray loud bl lacertae object s5 0716+ 714: Data and interpretation. arXiv preprint astro-ph/9706254 .
- Goswami, P., Sahayanathan, S., Sinha, A., Gogoi, R., 2020. Unfolding the X-ray spectral curvature of Mkn421 for further clues. *Monthly Notices of the Royal Astronomical Society* 499, 2094–2103. URL: <https://doi.org/10.1093/mnras/staa3022>, doi:10.1093/mnras/staa3022, arXiv:https://academic.oup.com/mnras/article-pdf/499/2/2094/339378
- Goswami, P., Sahayanathan, S., Sinha, A., Misra, R., Gogoi, R., 2018. Influence of energy-dependent particle diffusion on the X-ray spectral curvature of MKN421. *Monthly Notices of the Royal Astronomical Society* 480, 2046–2053. URL: <https://doi.org/10.1093/mnras/sty2003>, doi:10.1093/mnras/sty2003, arXiv:https://academic.oup.com/mnras/article-pdf/480/2/2046/254405
- Goyal, A., 2020. Blazar variability power spectra from radio up to tev photon energies: Mrk 421 and pks 2155- 304. *Monthly Notices of the Royal Astronomical Society* 494, 3432–3448.
- Hota, J., Shah, Z., Khatoon, R., Misra, R., Pradhan, A.C., Gogoi, R., 2021. Understanding the X-ray spectral curvature of Mkn 421 using broad-band AstroSat observations. *Monthly Notices of the Royal Astronomical Society* 508, 5921–5934. doi:10.1093/mnras/stab2903, arXiv:2110.03344.
- Jones, T.W., O’Dell, S.L., Stein, W.A., 1974. Physics of Compact Non-thermal Sources. I. Theory of Radiation Processes. *The Astrophysical Journal* 188, 353–368. doi:10.1086/152724.
- Kalberla, P.M.W., Burton, W.B., Hartmann, D., Arnal, E.M., Bajaja, E., Morras, R., Pöppel, W.G.L., 2005. The Leiden/Argentine/Bonn (LAB) Survey of Galactic HI. Final data release of the combined LDS and IAR surveys with improved stray-radiation corrections. *Astronomy & Astrophysics* 440, 775–782. doi:10.1051/0004-6361:

- 20041864, arXiv:astro-ph/0504140.
- Kapanadze, B., Vercellone, S., Romano, P., Hughes, P., Aller, M., Aller, H., Kharshiladze, O., Kapanadze, S., Tabagari, L., 2018. Swift Observations of Mrk 421 in Selected Epochs. I. The Spectral and Flux Variability in 2005-2008. *The Astrophysical Journal* 854, 66. doi:10.3847/1538-4357/aaa75d.
- Khatoon, R., Shah, Z., Hota, J., Misra, R., Gogoi, R., Pradhan, A.C., 2022. Correlations between X-ray spectral parameters of Mkn421 using long-term SwiftXRT data. *Monthly Notices of the Royal Astronomical Society* 515, 3749–3759. URL: <https://doi.org/10.1093/mnras/stac1964>, doi:10.1093/mnras/stac1964, arXiv:<https://academic.oup.com/mnras/article-pdf/515/3/3749/45291650/stac1964.pdf>
- Kirk, J.G., Rieger, F.M., Mastichiadis, A., 1998. Particle acceleration and synchrotron emission in blazar jets. *Astronomy & Astrophysics* 333, 452–458. doi:10.48550/arXiv.astro-ph/9801265, arXiv:astro-ph/9801265.
- Krawczynski, H., Sambruna, R., Kohnle, A., Coppi, P., Aharonian, F., Akhperjanian, A., Barrio, J., Bernlöhr, K., Börst, H., Bojahr, H., et al., 2001. Simultaneous x-ray and tev gamma-ray observation of the tev blazar markarian 421 during 2000 february and may. *The Astrophysical Journal* 559, 187.
- Lewis, T.R., Becker, P.A., Finke, J.D., 2016. Time-dependent electron acceleration in blazar transients: X-ray time lags and spectral formation. *The Astrophysical Journal* 824, 108. URL: <https://dx.doi.org/10.3847/0004-637X/824/2/108>, doi:10.3847/0004-637X/824/2/108.
- Lin, Y., Bertsch, D., Chiang, J., Fichtel, C., Hartman, R., Hunter, S., Kanbach, G., Kniffen, D., Kwok, P., Mattox, J., et al., 1992. Detection of high-energy gamma-ray emission from the bl lacertae object markarian 421 by the egret telescope on the compton observatory. *The Astrophysical Journal* 401, L61–L64.
- Macomb, D., Akerlof, C., Aller, H., Aller, M., Bertsch, D., Bruhweiler, F., Buckley, J., Carter-Lewis, D., Cawley, M., Cheng, K.P., et al., 1995. Multiwavelength observations of markarian 421 during a tev/x-ray flare. *The Astrophysical Journal* 449, L99.
- Mannheim, K., 1993. The proton blazar. *Astronomy and Astrophysics* 269, 67–76.
- Maraschi, L., Ghisellini, G., Celotti, A., 1992. A jet model for the gamma-ray emitting blazar 3c 279. *The Astrophysical Journal* 397, L5–L9.
- Markowitz, A.G., Nalewajko, K., Bhatta, G., Dewangan, G.C., Chandra, S., Dorner, D., Schleicher, B., Pajdosz-Śmierciak, U., Stawarz, L., Zola, S., Ostrowski, M., Carosati, D., Krishnan, S., Bachev, R., Benítez, E., Gazeas, K., Hiriart, D., Hu, S.M., Larionov, V., Marchini, A., Matsumoto, K., Nikiforova, A.A., Pursimo, T., Raiteri, C.M., Reichart, D.E., Rodriguez, D., Semkov, E., Strigachev, A., Sugiura, Y., Villata, M., Webb, J.R., Arbet-Engels, A., Baack, D., Balbo, M., Biland, A., Bretz, T., Buss, J., Eisenberger, L., Elsaesser, D., Hildebrand, D., Iotov, R., Kalenski, A., Mannheim, K., Mitchell, A., Neise, D., Noethe, M., Paravac, A., Rhode, W., Sliusar, V., Walter, R., 2022. Rapid X-ray variability in Mkn 421 during a multiwavelength campaign. *Monthly Notices of the Royal Astronomical Society* 513, 1662–1679. doi:10.1093/mnras/stac917, arXiv:2206.03874.
- Massaro, E., Perri, M., Giommi, P., Nesci, R., 2004. Log-parabolic spectra and particle acceleration in the BL Lac object Mkn 421: Spectral analysis of the complete BeppoSAX wide band X-ray data set. *Astronomy & Astrophysics* 413, 489–503. doi:10.1051/0004-6361:20031558, arXiv:astro-ph/0312260.
- Massaro, E., Tramacere, A., Perri, M., Giommi, P., Tosti, G., 2006. Log-parabolic spectra and particle acceleration in blazars. III. SSC emission in the TeV band from Mkn501. *Astronomy & Astrophysics* 448, 861–871. doi:10.1051/0004-6361:20053644, arXiv:astro-ph/0511673.
- Misra, R., Roy, J., Yadav, J., 2021. An alternative scheme to estimate astrosat/laxpc background for faint sources. *Journal of Astrophysics and Astronomy* 42, 55.
- Misra, R., Yadav, J.S., Verdhan Chauhan, J., Agrawal, P.C., Antia, H.M., Pahari, M., Chitnis, V.R., Dedhia, D., Katoch, T., Madhwani, P., Manchanda, R.K., Paul, B., Shah, P., 2017. AstroSat/LAXPC Observation of Cygnus X-1 in the Hard State. *The Astrophysical Journal* 835, 195. doi:10.3847/1538-4357/835/2/195, arXiv:1612.08793.
- Mücke, A., Protheroe, R., 2001. A proton synchrotron blazar model for flaring in markarian 501. *Astroparticle Physics* 15, 121–136.
- Petry, D., Bradbury, S., Konopelko, A., Fernandez, J., 1996. Detection of the gamma-rays from mkn 421 with the hegra cherenkov telescopes. arXiv preprint astro-ph/9606159.
- Punch, M., Akerlof, C.W., Cawley, M.F., Chantell, M., Fegan, D., Fennell, S., Gaidos, J., Hagan, J., Hillas, A., Jiang, Y., et al., 1992. Detection of tev photons from the active galaxy markarian 421. *nature* 358, 477–478.
- Rao, A.R., Bhattacharya, D., Bhalerao, V.B., Vadawale, S.V., Sreekumar, S., 2017. Cadmium-Zinc-Telluride Imager on-board AstroSat: a multi-faceted hard X-ray instrument. *Current Science* 113, 595. doi:10.1007/s12064-017-1131-0, arXiv:1710.10773.
- Rebillot, P.F., Badran, H.M., Blaylock, G., Bradbury, S.M., Buckley, J.H., Carter-Lewis, D.A., Celik, O., Chow, Y.C., Cogan, P., Cui, W., Daniel, M., Duke, C., Falcone, A., Fegan, S.J., Finley, J.P., Fortson, L.F., Gillanders, G.H., Grube, J., Gutierrez, K., Gyuk, G., Hanna, D., Holder, J., Horan, D., Hughes, S.B., Kenny, G.E., Kertzman, M., Kieda, D., Kildea, J., Kosack, K., Krawczynski, H., Krennrich, F., Lang, M.J., Le Bohec, S., Linton, E., Maier, G., Moriarty, P., Perkins, J., Pohl, M., Quinn, J., Ragan, K., Reynolds, P.T., Rose, H.J., Schroedter, M., Sembroski, G.H., Steele, G., Swordy, S.P., Valcarcel, L., Vassiliev, V.V., Wakely, S.P., Weekes, T.C., Zweerink, J., VERITAS Collaboration, Aller, M., Aller, H., Boltwood, P., Jung, I., Kranich, D., Nilsson, K., Pasanen, M., Sadun, A., Sillanpaa, A., 2006. Multiwavelength Observations of the Blazar Markarian 421 in 2002 December and 2003 January. *The Astrophysical Journal* 641, 740–751. doi:10.1086/500653, arXiv:astro-ph/0512628.
- Rybicki, G.B., Lightman, A.P., 1986. *Radiative Processes in Astrophysics*.
- Shah, Z., Ezhikode, S.H., Misra, R., Rajalakshmi, T.R., 2021. AstroSat observation of the HBL 1E595+650 during its October 2017 flaring. *Monthly Notices of the Royal Astronomical Society* 504, 5485–5495. doi:10.1093/mnras/stab1244, arXiv:2104.13472.
- Shah, Z., Sahayanathan, S., Mankuzhiyil, N., Kushwaha, P., Misra, R., Iqbal, N., 2017. Clues on high-energy emission mechanism from blazar 3C 454.3 during 2015 August flare. *Monthly Notices of the Royal Astronomical Society* 470, 3283–3299. URL: <https://doi.org/10.1093/mnras/stx1194>, doi:10.1093/mnras/stx1194, arXiv:<https://academic.oup.com/mnras/article-pdf/470/3/3283/185626>
- Shukla, A., Chitnis, V., Vishwanath, P., Acharya, B., Anupama, G., Bhattacharjee, P., Britto, R., Prabhu, T., Saha, L., Singh, B., 2012. Multiwavelength study of the tev blazar mrk 421 during a giant flare. *Astronomy & Astrophysics* 541, A140.
- Sikora, M., Begelman, M.C., Rees, M.J., 1994. Comptonization of diffuse ambient radiation by a relativistic jet: The source of gamma rays from blazars? *The Astrophysical Journal* 421, 153–162.
- Singh, K.P., Stewart, G.C., Chandra, S., Mukerjee, K., Kotak, S., Beardmore, A.P., Chitnis, V., Dewangan, G.C., Bhattacharyya, S., Mirza, I., Kamble, N., Navalkar, V., Shah, H., Vishwakarma, S., Koyande, J., 2016. In-orbit performance of SXT aboard AstroSat, in: den Herder, J.W.A., Takahashi, T., Bautz, M. (Eds.), *Space Telescopes and Instrumentation 2016: Ultraviolet to Gamma Ray*, p. 99051E. doi:10.1117/12.2235309.
- Singh, K.P., Stewart, G.C., Westergaard, N.J., Bhattacharaya, S., Chandra, S., Chitnis, V.R., Dewangan, G.C., Kothare, A.T., Mirza, I.M., Mukerjee, K., Navalkar, V., Shah, H., Abbey, A.F., Beardmore, A.P., Kotak, S., Kamble, N., Vishwakarma, S., Pathare, D.P., Risbud, V.M., Koyande, J.P., Stevenson, T., Bicknell, C., Crawford, T., Hansford, G., Peters, G., Sykes, J., Agarwal, P., Sebastian, M., Rajarajan, A., Nagesh, G., Narendra, S., Ramesh, M., Rai, R., Navalgund, K.H., Sarma, K.S., Pandiyar, R., Subbarao, K., Gupta, T., Thakkar, N., Singh, A.K., Bajpai, A., 2017. Soft X-ray Focusing Telescope Aboard AstroSat: Design, Characteristics and Performance. *Journal of Astrophysics and Astronomy* 38, 29. doi:10.1007/s12036-017-9448-7.
- Sinha, A., Shukla, A., Saha, L., Acharya, B., Anupama, G., Bhattacharjee, P., Britto, R., Chitnis, V., Prabhu, T., Singh, B., et al., 2016. Long-term study of mkn 421 with the hagar array of telescopes. *Astronomy & Astrophysics* 591, A83.
- Tandon, S.N., Hutchings, J.B., Ghosh, S.K., Subramaniam, A., Koshy, G., Girish, V., Kamath, P.U., Kathiravan, S., Kumar, A., Lancelot, J.P., Mahesh, P.K., Mohan, R., Murthy, J., Nagabhushana, S., Pati, A.K., Postma, J., Rao, N.K., Sankarasubramanian, K., Sreekumar, P.,

Sriram, S., Stalin, C.S., Sutaria, F., Sreedhar, Y.H., Barve, I.V., Mondal, C., Sahu, S., 2017a. In-orbit Performance of UVIT and First Results. *Journal of Astrophysics and Astronomy* 38, 28. doi:10.1007/s12036-017-9445-x, arXiv:1612.00612.

Tandon, S.N., Subramaniam, A., Girish, V., Postma, J., Sankarasubramanian, K., Sriram, S., Stalin, C.S., Mondal, C., Sahu, S., Joseph, P., Hutchings, J., Ghosh, S.K., Barve, I.V., George, K., Kamath, P.U., Kathiravan, S., Kumar, A., Lancelot, J.P., Leahy, D., Mahesh, P.K., Mohan, R., Nagabhushana, S., Pati, A.K., Kameswara Rao, N., Sreedhar, Y.H., Sreekumar, P., 2017b. In-orbit Calibrations of the Ultraviolet Imaging Telescope. *AJ* 154, 128. doi:10.3847/1538-3881/aa8451, arXiv:1705.03715.

Tramacere, A., Massaro, F., Cavaliere, A., 2007. Signatures of synchrotron emission and of electron acceleration in the x-ray spectra of mrk 421. *Astronomy & Astrophysics* 466, 521–529.

Ulrich, M.H., Maraschi, L., Urry, C.M., 1997. Variability of Active Galactic Nuclei. *Annual Review of Astronomy and Astrophysics* 35, 445–502. doi:10.1146/annurev.astro.35.1.445.

Urry, C.M., Padovani, P., 1995. Unified Schemes for Radio-Loud Active Galactic Nuclei. *Publications of the Astronomical Society of the Pacific* 107, 803. doi:10.1086/133630, arXiv:astro-ph/9506063.

Wagner, S.J., Witzel, A., 1995. Intraday variability in quasars and bl lac objects. *Annual Review of Astronomy and Astrophysics* 33, 163–197. URL: <https://doi.org/10.1146/annurev.aa.33.090195.001115>, doi:10.1146/annurev.aa.33.090195.001115, arXiv:<https://doi.org/10.1146/annurev.aa.33.090195.001115>.

Yadav, J.S., Agrawal, P.C., Antia, H.M., Chauhan, J.V., Dedhia, D., Katoch, T., Madhwani, P., Manchanda, R.K., Misra, R., Pahari, M., Paul, B., Shah, P., 2016. Large Area X-ray Proportional Counter (LAXPC) instrument onboard ASTROSAT, in: den Herder, J.W.A., Takahashi, T., Bautz, M. (Eds.), *Space Telescopes and Instrumentation 2016: Ultraviolet to Gamma Ray*, p. 99051D. doi:10.1117/12.2231857.

5. Appendix

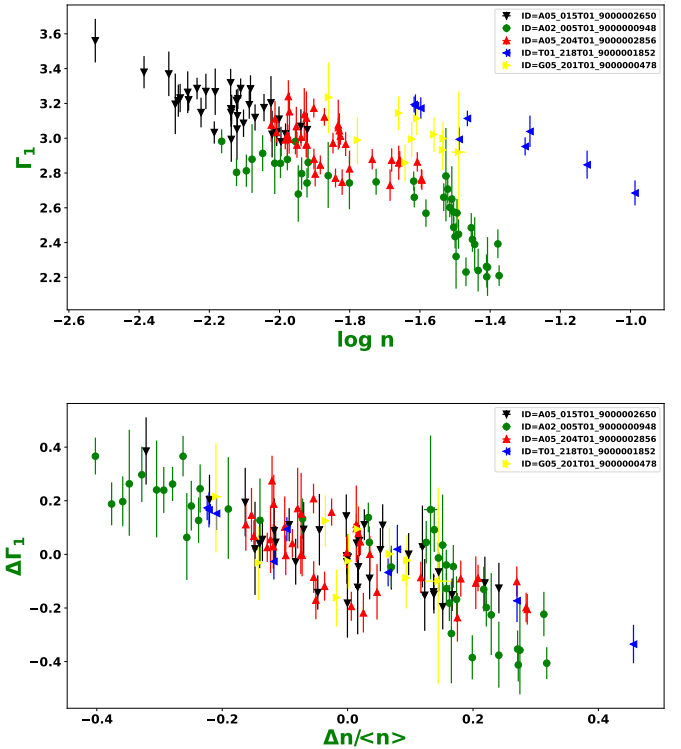


Figure 6: Variation of spectral index Γ_1 and particle density $\langle n \rangle$ in BPL model. The upper pannel represents relationship between Γ_1 and $\log n$. The lower pannel represents correlation bewteen index ($\Delta\Gamma_1$) and the normalized particle density ($\Delta n / \langle n \rangle$) at $\xi = \xi_{ref}$.

Table 6: The best fit parameter values obtained by fitting time-resolved broadband X-ray spectra of S1 observation with the synchrotron convolved BPL/LP/ $\xi - max$ models.

Time	Broken Power law					Log parabola				$\xi - max$ model		
	Γ_1	Γ_2	norm (n) ($\times 10^{-2}$)	χ^2_{dof}	α	β	norm (n) ($\times 10^{-2}$)	χ^2_{dof}	p	ξ_{max}	norm (n) ($\times 10^{-2}$)	χ^2_{dof}
5000	$3.13^{+0.10}_{-0.10}$	$4.32^{+0.11}_{-0.11}$	$15.96^{+0.41}_{-0.41}$	1.03	$3.19^{+0.10}_{-0.10}$	$1.17^{+0.20}_{-0.18}$	$34.27^{+0.66}_{-0.65}$	1.04	$3.08^{+0.10}_{-0.09}$	$6.14^{+0.86}_{-0.64}$	$38.67^{+0.88}_{-0.88}$	1.05
15000	$3.02^{+0.09}_{-0.09}$	$4.13^{+0.11}_{-0.11}$	$18.15^{+0.39}_{-0.39}$	1.00	$3.02^{+0.09}_{-0.09}$	$1.11^{+0.18}_{-0.17}$	$37.93^{+0.67}_{-0.66}$	1.02	$2.96^{+0.08}_{-0.08}$	$6.24^{+0.85}_{-0.64}$	$41.93^{+0.88}_{-0.87}$	1.03
25000	$3.23^{+0.06}_{-0.06}$	$4.87^{+0.13}_{-0.12}$	$18.09^{+0.3}_{-0.3}$	1.09	$3.29^{+0.06}_{-0.06}$	$1.58^{+0.17}_{-0.16}$	$40.73^{+0.61}_{-0.60}$	1.14	$3.05^{+0.06}_{-0.06}$	$4.76^{+0.35}_{-0.29}$	$47.73^{+0.82}_{-0.82}$	1.12
35000	$3.21^{+0.06}_{-0.06}$	$5.06^{+0.14}_{-0.13}$	$19.44^{+0.32}_{-0.32}$	1.16	$3.28^{+0.06}_{-0.06}$	$1.78^{+0.18}_{-0.17}$	$44.07^{+0.67}_{-0.66}$	1.22	$3.03^{+0.06}_{-0.06}$	$4.44^{+0.30}_{-0.25}$	$51.88^{+0.89}_{-0.88}$	1.20
45000	$3.14^{+0.08}_{-0.08}$	$5.03^{+0.15}_{-0.14}$	$19.96^{+0.42}_{-0.42}$	0.94	$3.15^{+0.09}_{-0.09}$	$1.96^{+0.22}_{-0.21}$	$45.09^{+0.80}_{-0.79}$	0.98	$2.97^{+0.07}_{-0.07}$	$4.35^{+0.32}_{-0.27}$	$51.97^{+1.04}_{-1.02}$	0.97
55000	$3.10^{+0.10}_{-0.09}$	$4.94^{+0.19}_{-0.17}$	$19.99^{+0.49}_{-0.49}$	0.94	$3.13^{+0.10}_{-0.10}$	$1.84^{+0.26}_{-0.25}$	$44.41^{+0.95}_{-0.92}$	1.00	$2.94^{+0.09}_{-0.08}$	$4.37^{+0.42}_{-0.34}$	$51.10^{+1.21}_{-1.19}$	0.96

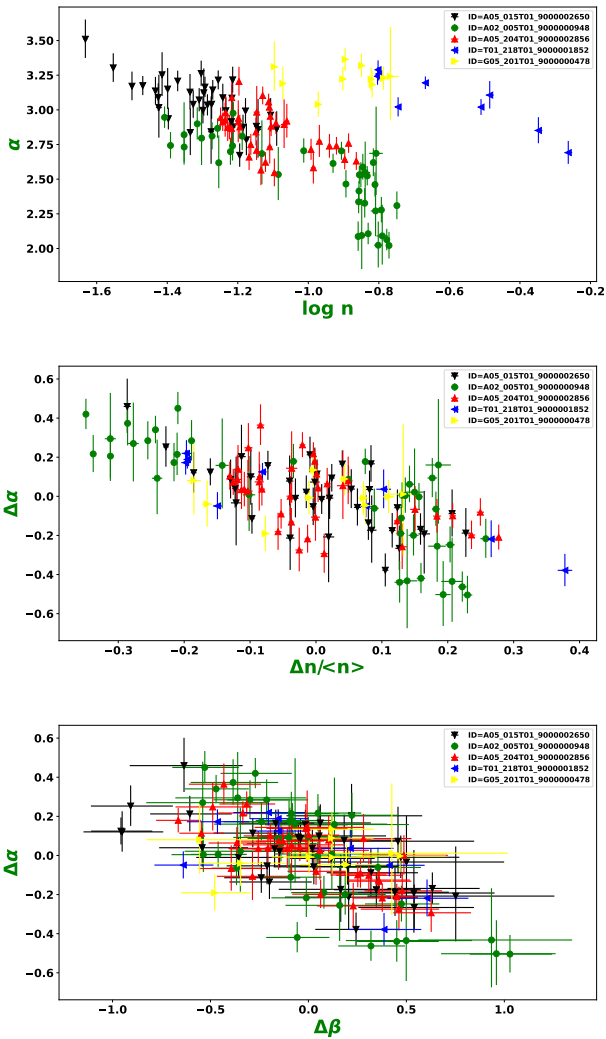


Figure 7: The correlations between the spectral parameters obtained by fitting the synchrotron convolved LP model to the joint SXT and LAXPC spectrum in each time segment. Different colors in the plot depicts individual observations. The Upper panel represents variation of α with $\log(n)$ at $\xi = \xi_{ref}$. The middle panel represents correlation between $\Delta\alpha$ and $\Delta n / \langle n \rangle$. The Bottom panel represents correlation between $\Delta\alpha$ and $\Delta\beta$.

Table 7: The best fit parameter values obtained by fitting time-resolved broadband X-ray spectra of S2 observation with the synchrotron convolved BPL/LP/ ξ - *max* models.

Time	Broken Power law					Log parabola				ξ - <i>max</i> model		
	Γ_1	Γ_2	norm (n) ($\times 10^{-2}$)	$\frac{\chi^2}{dof}$	α	β	norm (n) ($\times 10^{-2}$)	$\frac{\chi^2}{dof}$	p	ξ_{max}	norm (n) ($\times 10^{-2}$)	$\frac{\chi^2}{dof}$
5000	2.90 ^{+0.08} _{-0.08}	4.70 ^{+0.16} _{-0.15}	11.97 ^{+0.19} _{-0.19}	1.03	2.74 ^{+0.10} _{-0.09}	1.81 ^{+0.22} _{-0.21}	24.89 ^{+0.42} _{-0.42}	1.06	2.70 ^{+0.07} _{-0.07}	4.39 ^{+0.33} _{-0.28}	26.95 ^{+0.60} _{-0.59}	1.05
15000	2.91 ^{+0.09} _{-0.09}	4.84 ^{+0.16} _{-0.15}	12.31 ^{+0.22} _{-0.22}	0.93	2.73 ^{+0.12} _{-0.11}	1.98 ^{+0.24} _{-0.22}	25.87 ^{+0.46} _{-0.46}	0.95	2.71 ^{+0.08} _{-0.07}	4.27 ^{+0.31} _{-0.26}	28.06 ^{+0.72} _{-0.70}	0.96
25000	2.98 ^{+0.07} _{-0.07}	4.57 ^{+0.14} _{-0.14}	11.48 ^{+0.17} _{-0.17}	1.04	2.95 ^{+0.08} _{-0.08}	1.49 ^{+0.19} _{-0.18}	24.47 ^{+0.38} _{-0.37}	1.06	2.85 ^{+0.06} _{-0.06}	4.98 ^{+0.43} _{-0.35}	27.18 ^{+0.49} _{-0.50}	1.07
35000	2.91 ^{+0.10} _{-0.10}	4.42 ^{+0.16} _{-0.15}	12.90 ^{+0.26} _{-0.26}	1.14	2.90 ^{+0.12} _{-0.11}	1.38 ^{+0.23} _{-0.22}	26.85 ^{+0.52} _{-0.51}	1.18	2.81 ^{+0.09} _{-0.09}	5.13 ^{+0.59} _{-0.46}	29.61 ^{+0.74} _{-0.73}	1.16
45000	2.88 ^{+0.20} _{-0.19}	4.32 ^{+0.16} _{-0.15}	12.51 ^{+0.47} _{-0.46}	0.78	2.82 ^{+0.23} _{-0.22}	1.40 ^{+0.35} _{-0.32}	25.87 ^{+0.84} _{-0.84}	0.78	2.84 ^{+0.17} _{-0.16}	5.49 ^{+1.10} _{-0.73}	28.42 ^{+1.23} _{-1.11}	0.81
55000	2.86 ^{+0.18} _{-0.18}	4.11 ^{+0.15} _{-0.15}	13.35 ^{+0.45} _{-0.44}	0.95	2.80 ^{+0.21} _{-0.19}	1.22 ^{+0.32} _{-0.29}	27.18 ^{+0.82} _{-0.82}	0.95	2.87 ^{+0.16} _{-0.15}	6.27 ^{+1.54} _{-0.96}	29.57 ^{+1.06} _{-1.01}	1.00
65000	2.74 ^{+0.09} _{-0.08}	4.35 ^{+0.13} _{-0.13}	14.64 ^{+0.23} _{-0.23}	0.95	2.70 ^{+0.10} _{-0.10}	1.52 ^{+0.20} _{-0.19}	29.50 ^{+0.50} _{-0.49}	0.98	2.67 ^{+0.07} _{-0.07}	4.84 ^{+0.41} _{-0.34}	31.65 ^{+0.73} _{-0.71}	0.97
75000	2.80 ^{+0.09} _{-0.09}	4.55 ^{+0.17} _{-0.16}	14.41 ^{+0.26} _{-0.26}	0.80	2.74 ^{+0.11} _{-0.11}	1.67 ^{+0.24} _{-0.23}	29.68 ^{+0.56} _{-0.55}	0.81	2.71 ^{+0.08} _{-0.08}	4.61 ^{+0.43} _{-0.35}	32.14 ^{+0.80} _{-0.78}	0.81
85000	2.88 ^{+0.06} _{-0.06}	4.31 ^{+0.13} _{-0.12}	13.84 ^{+0.18} _{-0.18}	1.01	2.87 ^{+0.07} _{-0.07}	1.29 ^{+0.17} _{-0.16}	28.44 ^{+0.41} _{-0.40}	1.05	2.78 ^{+0.06} _{-0.06}	5.24 ^{+0.45} _{-0.37}	31.13 ^{+0.53} _{-0.53}	1.02
95000	2.86 ^{+0.09} _{-0.08}	4.39 ^{+0.13} _{-0.13}	13.57 ^{+0.22} _{-0.22}	1.01	2.81 ^{+0.10} _{-0.10}	1.46 ^{+0.20} _{-0.19}	28.01 ^{+0.47} _{-0.47}	1.02	2.77 ^{+0.07} _{-0.07}	5.09 ^{+0.47} _{-0.38}	30.51 ^{+0.66} _{-0.65}	1.04
105000	2.68 ^{+0.17} _{-0.16}	4.39 ^{+0.15} _{-0.14}	14.28 ^{+0.38} _{-0.37}	0.85	2.62 ^{+0.20} _{-0.18}	1.66 ^{+0.31} _{-0.28}	28.54 ^{+0.77} _{-0.79}	0.86	2.67 ^{+0.13} _{-0.12}	4.81 ^{+0.60} _{-0.46}	30.61 ^{+1.33} _{-1.19}	0.89
115000	2.98 ^{+0.08} _{-0.07}	4.34 ^{+0.13} _{-0.12}	14.16 ^{+0.23} _{-0.22}	0.91	2.98 ^{+0.08} _{-0.08}	1.23 ^{+0.17} _{-0.17}	29.72 ^{+0.46} _{-0.45}	0.94	2.87 ^{+0.07} _{-0.07}	5.53 ^{+0.55} _{-0.44}	32.94 ^{+0.61} _{-0.62}	0.93
125000	2.86 ^{+0.09} _{-0.09}	4.48 ^{+0.14} _{-0.14}	14.68 ^{+0.26} _{-0.26}	0.87	2.81 ^{+0.11} _{-0.10}	1.55 ^{+0.21} _{-0.20}	30.50 ^{+0.54} _{-0.53}	0.89	2.76 ^{+0.08} _{-0.07}	4.89 ^{+0.45} _{-0.36}	33.28 ^{+0.76} _{-0.75}	0.89
135000	2.78 ^{+0.19} _{-0.19}	4.68 ^{+0.18} _{-0.17}	15.55 ^{+0.53} _{-0.52}	1.03	2.68 ^{+0.24} _{-0.22}	1.89 ^{+0.38} _{-0.34}	32.25 ^{+0.99} _{-1.01}	1.06	2.73 ^{+0.15} _{-0.14}	4.51 ^{+0.60} _{-0.44}	35.04 ^{+1.74} _{-1.54}	1.05
145000	2.74 ^{+0.16} _{-0.15}	4.46 ^{+0.15} _{-0.14}	16.52 ^{+0.44} _{-0.44}	1.04	2.53 ^{+0.20} _{-0.18}	1.88 ^{+0.32} _{-0.29}	33.79 ^{+1.01} _{-0.95}	1.04	2.72 ^{+0.12} _{-0.12}	4.84 ^{+0.60} _{-0.45}	36.30 ^{+1.42} _{-1.29}	1.09
155000	2.75 ^{+0.08} _{-0.07}	4.53 ^{+0.14} _{-0.13}	17.82 ^{+0.25} _{-0.25}	0.86	2.70 ^{+0.09} _{-0.09}	1.68 ^{+0.20} _{-0.19}	36.31 ^{+0.57} _{-0.57}	0.91	2.67 ^{+0.06} _{-0.06}	4.56 ^{+0.33} _{-0.28}	38.99 ^{+0.82} _{-0.81}	0.90
165000	2.66 ^{+0.06} _{-0.06}	4.37 ^{+0.12} _{-0.11}	19.87 ^{+0.22} _{-0.22}	1.05	2.61 ^{+0.07} _{-0.07}	1.61 ^{+0.17} _{-0.16}	39.46 ^{+0.53} _{-0.52}	1.09	2.63 ^{+0.05} _{-0.05}	4.71 ^{+0.30} _{-0.26}	41.85 ^{+0.70} _{-0.69}	1.08
175000	2.57 ^{+0.08} _{-0.08}	4.71 ^{+0.15} _{-0.14}	20.54 ^{+0.28} _{-0.28}	0.95	2.46 ^{+0.10} _{-0.10}	2.11 ^{+0.22} _{-0.21}	40.93 ^{+0.68} _{-0.67}	0.98	2.54 ^{+0.06} _{-0.06}	4.08 ^{+0.24} _{-0.20}	42.52 ^{+1.05} _{-1.02}	0.98
185000	2.75 ^{+0.06} _{-0.05}	4.52 ^{+0.12} _{-0.11}	19.83 ^{+0.22} _{-0.22}	0.99	2.70 ^{+0.07} _{-0.06}	1.67 ^{+0.16} _{-0.15}	40.41 ^{+0.52} _{-0.51}	1.03	2.68 ^{+0.05} _{-0.05}	4.65 ^{+0.27} _{-0.24}	43.40 ^{+0.68} _{-0.68}	1.03
195000	2.60 ^{+0.06} _{-0.06}	4.48 ^{+0.11} _{-0.11}	21.98 ^{+0.23} _{-0.23}	1.05	2.52 ^{+0.07} _{-0.07}	1.81 ^{+0.16} _{-0.16}	43.48 ^{+0.57} _{-0.56}	1.10	2.57 ^{+0.04} _{-0.04}	4.42 ^{+0.23} _{-0.20}	45.49 ^{+0.79} _{-0.78}	1.08
205000	2.71 ^{+0.08} _{-0.08}	4.50 ^{+0.13} _{-0.12}	21.85 ^{+0.33} _{-0.33}	1.05	2.62 ^{+0.10} _{-0.10}	1.76 ^{+0.20} _{-0.19}	44.24 ^{+0.73} _{-0.73}	1.09	2.65 ^{+0.07} _{-0.06}	4.59 ^{+0.33} _{-0.27}	47.11 ^{+1.11} _{-1.07}	1.08
215000	2.66 ^{+0.08} _{-0.08}	4.32 ^{+0.11} _{-0.11}	21.61 ^{+0.30} _{-0.30}	1.02	2.59 ^{+0.10} _{-0.09}	1.62 ^{+0.18} _{-0.17}	42.94 ^{+0.69} _{-0.68}	1.03	2.63 ^{+0.06} _{-0.06}	4.80 ^{+0.34} _{-0.29}	45.42 ^{+1.02} _{-0.99}	1.04
225000	2.65 ^{+0.19} _{-0.18}	4.06 ^{+0.12} _{-0.12}	22.11 ^{+0.66} _{-0.64}	1.01	2.55 ^{+0.22} _{-0.21}	1.41 ^{+0.31} _{-0.28}	43.23 ^{+1.41} _{-1.48}	1.02	2.73 ^{+0.14} _{-0.14}	5.78 ^{+1.05} _{-0.72}	46.30 ^{+2.01} _{-1.79}	1.05
235000	2.57 ^{+0.08} _{-0.08}	3.88 ^{+0.11} _{-0.10}	22.44 ^{+0.30} _{-0.30}	1.08	2.53 ^{+0.09} _{-0.09}	1.22 ^{+0.17} _{-0.16}	42.70 ^{+0.71} _{-0.71}	1.10	2.58 ^{+0.06} _{-0.06}	5.53 ^{+0.52} _{-0.42}	44.72 ^{+0.99} _{-0.97}	1.11
245000	2.49 ^{+0.08} _{-0.08}	3.87 ^{+0.11} _{-0.10}	23.37 ^{+0.31} _{-0.31}	1.00	2.46 ^{+0.09} _{-0.09}	1.39 ^{+0.13} _{-0.13}	44.44 ^{+0.59} _{-0.60}	1.38	2.52 ^{+0.06} _{-0.06}	5.32 ^{+0.48} _{-0.39}	45.33 ^{+1.10} _{-1.06}	1.03
255000	2.58 ^{+0.06} _{-0.06}	3.97 ^{+0.10} _{-0.10}	22.22 ^{+0.23} _{-0.23}	1.00	2.53 ^{+0.07} _{-0.06}	1.30 ^{+0.15} _{-0.14}	42.51 ^{+0.55} _{-0.55}	1.03	2.57 ^{+0.04} _{-0.04}	5.25 ^{+0.38} _{-0.32}	44.48 ^{+0.72} _{-0.70}	1.02
265000	2.49 ^{+0.06} _{-0.06}	4.23 ^{+0.11} _{-0.10}	22.23 ^{+0.22} _{-0.22}	0.94	2.41 ^{+0.07} _{-0.07}	1.67 ^{+0.16} _{-0.15}	42.47 ^{+0.56} _{-0.55}	0.97	2.51 ^{+0.04} _{-0.04}	4.62 ^{+0.26} _{-0.22}	43.83 ^{+0.77} _{-0.76}	0.97
275000	2.43 ^{+0.07} _{-0.07}	4.30 ^{+0.11} _{-0.11}	22.32 ^{+0.25} _{-0.25}	0.92	2.34 ^{+0.09} _{-0.08}	1.84 ^{+0.17} _{-0.17}	42.43 ^{+0.63} _{-0.63}	0.95	2.48 ^{+0.05} _{-0.05}	4.46 ^{+0.24} _{-0.21}	43.43 ^{+0.93} _{-0.91}	0.96
285000	2.45 ^{+0.09} _{-0.08}	4.39 ^{+0.12} _{-0.12}	22.54 ^{+0.30} _{-0.30}	0.97	2.33 ^{+0.11} _{-0.10}	1.95 ^{+0.21} _{-0.20}	43.17 ^{+0.76} _{-0.77}	1.00	2.49 ^{+0.06} _{-0.06}	4.37 ^{+0.27} _{-0.23}	44.34 ^{+1.18} _{-1.14}	1.01
295000	2.39 ^{+0.08} _{-0.08}	4.19 ^{+0.11} _{-0.10}	25.21 ^{+0.32} _{-0.32}	0.97	2.31 ^{+0.10} _{-0.10}	1.75 ^{+0.19} _{-0.18}	47.29 ^{+0.82} _{-0.83}	1.00	2.45 ^{+0.06} _{-0.05}	4.54 ^{+0.28} _{-0.24}	48.14 ^{+1.28} _{-1.24}	1.00
305000	2.39 ^{+0.16} _{-0.15}	4.30 ^{+0.12} _{-0.12}	23.60 ^{+0.51} _{-0.51}	0.99	2.27 ^{+0.19} _{-0.18}	1.92 ^{+0.30} _{-0.28}	44.52 ^{+1.30} _{-1.36}	1.01	2.49 ^{+0.10} _{-0.10}	4.49 ^{+0.42} _{-0.33}	45.89 ^{+2.19} _{-2.02}	1.03
315000	2.26 ^{+0.17} _{-0.17}	4.44 ^{+0.13} _{-0.13}	24.48 ^{+0.54} _{-0.54}	0.82	2.09 ^{+0.22} _{-0.21}	2.26 ^{+0.34} _{-0.31}	45.37 ^{+1.52} _{-1.64}	0.83	2.44 ^{+0.11} _{-0.10}	4.24 ^{+0.36} _{-0.30}	46.43 ^{+2.52} _{-2.33}	0.90
325000	2.23 ^{+0.08} _{-0.08}	4.41 ^{+0.12} _{-0.12}	23.02 ^{+0.28} _{-0.28}	1.05	2.09 ^{+0.11} _{-0.10}	2.21 ^{+0.21} _{-0.20}	42.37 ^{+0.77} _{-0.78}	1.08	2.36 ^{+0.05} _{-0.05}	4.04 ^{+0.21} _{-0.17}	41.96 ^{+1.19} _{-1.16}	1.11
335000	2.20 ^{+0.06} _{-0.06}	3.96 ^{+0.10} _{-0.10}	24.43 ^{+0.25} _{-0.25}	0.86	2.11 ^{+0.08} _{-0.08}	1.70 ^{+0.16} _{-0.16}	43.59 ^{+0.64} _{-0.64}	0.90	2.34 ^{+0.04} _{-0.04}	4.58 ^{+0.26} _{-0.22}	43.44 ^{+0.89} _{-0.88}	0.89
345000	2.21 ^{+0.06} _{-0.06}	4.27 ^{+0.11} _{-0.10}	25.30 ^{+0.24} _{-0.24}	0.95	2.06 ^{+0.08} _{-0.08}	2.08 ^{+0.17} _{-0.17}	45.95 ^{+0.65} _{-0.65}	0.98	2.34 ^{+0.04} _{-0.04}	4.16 ^{+0.17} _{-0.17}	45.35 ^{+0.92} _{-0.91}	1.00
355000	2.78 ^{+0.28} _{-0.26}	4.47 ^{+0.15} _{-0.15}	21.74 ^{+1.10} _{-1.05}	0.72	2.69 ^{+0.34} _{-0.30}	1.69 ^{+0.47} _{-0.41}	44.59 ^{+1.89} _{-1.95}	0.73	2.89 ^{+0.21} _{-0.20}	5.50 ^{+1.30} _{-0.81}	49.09 ^{+2.53} _{-2.27}	0.82
365000	2.42 ^{+0.07} _{-0.07}	4.62 ^{+0.12} _{-0.11}	23.45 ^{+0.27} _{-0.27}	0.93	2.28 ^{+0.09} _{-0.09}	2.23 ^{+0.19} _{-0.19}	45.25 ^{+0.70} _{-0.70}	0.95	2.46 ^{+0.05} _{-0.05}	4.05 ^{+0.20} _{-0.17}	45.88 ^{+1.08} _{-1.06}	1.00
375000	2.26 ^{+0.07} _{-0.07}	4.89 ^{+0.13} _{-0.12}	24.41 ^{+0.25} _{-0.25}	0.83	2.02 ^{+0.10} _{-0.09}	2.79 ^{+0.21} _{-0.20}	46.24 ^{+0.73} _{-0.73}	0.87	2.36 ^{+0.04} _{-0.04}	3.66 ^{+0.14} _{-0.13}	45.33 ^{+1.12} _{-1.10}	0.88
385000	2.24 ^{+0.13} _{-0.12}	4.81 ^{+0.15} _{-0.14}	23.83 ^{+0.39} _{-0.40}	0.86	2.02 ^{+0.07} _{-0.06}	2.72 ^{+0.30} _{-0.28}	44.86 ^{+1.14} _{-1.19}	0.86	2.37 ^{+0.08} _{-0.07}	3.74 ^{+0.22} _{-0.19}	44.53 ^{+1.93} _{-1.85}	0.95
395000	2.32 ^{+0.19} _{-0.19}	4.84 ^{+0.16} _{-0.15}	22.38 ^{+0.58} _{-0.57}	0.90	2.09 ^{+0.16} _{-0.16}	2.69 ^{+0.41} _{-0.37}	42.80 ^{+1.55} _{-1.69}	0.89	2.49 ^{+0.12} _{-0.11}	3.95 ^{+0.34} _{-0.28}	44.36 ^{+2.62} _{-2.42}	1.02

Table 8: The best fit parameter values obtained by fitting time-resolved broadband X-ray spectra of S3 observation with the synchrotron convolved BPL/LP/ $\zeta - max$ models.

Time	Broken Power law				Log parabola				$\zeta - max$ model			
	Γ_1	Γ_2	norm (n) ($\times 10^{-2}$)	$\frac{\chi^2}{dof}$	α	β	norm (n) ($\times 10^{-2}$)	$\frac{\chi^2}{dof}$	p	ζ_{max}	norm (n) ($\times 10^{-2}$)	$\frac{\chi^2}{dof}$
5000	2.58 ^{+0.07} _{-0.07}	4.94 ^{+0.12} _{-0.11}	37.26 ^{+0.55} _{-0.55}	1.16	2.69 ^{+0.08} _{-0.08}	2.30 ^{+0.19} _{-0.18}	76.88 ^{+1.11} _{-1.09}	1.23	2.65 ^{+0.05} _{-0.05}	3.90 ^{+0.18} _{-0.16}	81.75 ^{+1.58} _{-1.63}	1.22
15000	2.75 ^{+0.08} _{-0.08}	5.28 ^{+0.13} _{-0.12}	32.50 ^{+0.59} _{-0.59}	0.78	2.85 ^{+0.10} _{-0.09}	2.52 ^{+0.21} _{-0.20}	70.64 ^{+1.11} _{-1.09}	0.82	2.75 ^{+0.06} _{-0.06}	3.78 ^{+0.18} _{-0.16}	77.20 ^{+1.59} _{-1.63}	0.85
25000	3.04 ^{+0.09} _{-0.09}	5.19 ^{+0.14} _{-0.14}	27.62 ^{+0.63} _{-0.63}	1.04	3.11 ^{+0.10} _{-0.10}	2.13 ^{+0.22} _{-0.21}	61.53 ^{+1.12} _{-1.11}	1.05	2.89 ^{+0.08} _{-0.07}	4.08 ^{+0.22} _{-0.22}	70.21 ^{+1.47} _{-1.47}	1.13
35000	2.95 ^{+0.05} _{-0.05}	5.37 ^{+0.14} _{-0.14}	27.24 ^{+0.36} _{-0.36}	1.03	3.02 ^{+0.06} _{-0.06}	2.33 ^{+0.18} _{-0.17}	60.03 ^{+0.82} _{-0.80}	1.11	2.79 ^{+0.04} _{-0.04}	3.74 ^{+0.16} _{-0.15}	67.54 ^{+0.99} _{-0.98}	1.08
45000	3.11 ^{+0.04} _{-0.04}	5.03 ^{+0.12} _{-0.12}	23.11 ^{+0.29} _{-0.29}	1.04	3.19 ^{+0.05} _{-0.04}	1.77 ^{+0.15} _{-0.14}	51.27 ^{+0.65} _{-0.63}	1.14	2.93 ^{+0.04} _{-0.04}	4.31 ^{+0.23} _{-0.20}	59.42 ^{+0.81} _{-0.80}	1.11
55000	3.19 ^{+0.07} _{-0.07}	5.06 ^{+0.15} _{-0.14}	19.93 ^{+0.36} _{-0.36}	1.06	3.29 ^{+0.07} _{-0.07}	1.71 ^{+0.19} _{-0.18}	44.83 ^{+0.74} _{-0.72}	1.12	2.99 ^{+0.06} _{-0.06}	4.38 ^{+0.31} _{-0.26}	52.77 ^{+0.96} _{-0.95}	1.10
65000	3.19 ^{+0.05} _{-0.05}	5.06 ^{+0.12} _{-0.12}	19.86 ^{+0.26} _{-0.26}	0.89	3.26 ^{+0.05} _{-0.05}	1.76 ^{+0.15} _{-0.15}	44.91 ^{+0.57} _{-0.56}	0.95	3.01 ^{+0.04} _{-0.04}	4.47 ^{+0.25} _{-0.22}	52.55 ^{+0.76} _{-0.75}	0.94
75000	3.17 ^{+0.06} _{-0.06}	4.72 ^{+0.12} _{-0.12}	20.24 ^{+0.34} _{-0.34}	1.04	3.24 ^{+0.06} _{-0.06}	1.45 ^{+0.16} _{-0.16}	44.76 ^{+0.67} _{-0.66}	1.07	3.02 ^{+0.06} _{-0.06}	5.01 ^{+0.39} _{-0.33}	51.73 ^{+0.89} _{-0.89}	1.09
85000	2.99 ^{+0.07} _{-0.07}	4.32 ^{+0.10} _{-0.10}	22.58 ^{+0.37} _{-0.37}	1.01	3.02 ^{+0.07} _{-0.07}	1.28 ^{+0.15} _{-0.15}	47.46 ^{+0.69} _{-0.68}	1.04	2.91 ^{+0.06} _{-0.06}	5.51 ^{+0.48} _{-0.39}	52.73 ^{+0.89} _{-0.87}	1.04

Table 9: The best fit parameter values obtained by fitting time-resolved broadband X-ray spectra of S4 observation with the sncrotron convolved BPL/LP/ $\xi - max$ models.

Time	Broken Power law					Log parabola				$\xi - max$ model		
	Γ_1	Γ_2	norm (n) ($\times 10^{-2}$)	$\frac{\chi^2}{dof}$	α	β	norm (n) ($\times 10^{-2}$)	$\frac{\chi^2}{dof}$	p	ξ_{max}	norm (n) ($\times 10^{-2}$)	$\frac{\chi^2}{dof}$
5000	3.35 ^{+0.08} _{-0.08}	5.02 ^{+0.21} _{-0.23}	11.79 ^{+0.22} _{-0.22}	0.98	3.04 ^{+0.1} _{-0.1}	1.6 ^{+0.23} _{-0.22}	26.55 ^{+0.49} _{-0.48}	0.99	2.92 ^{+0.08} _{-0.08}	4.87 ^{+0.5} _{-0.39}	29.99 ^{+0.65} _{-0.66}	1.00
15000	3.25 ^{+0.09} _{-0.08}	4.89 ^{+0.22} _{-0.24}	10.82 ^{+0.21} _{-0.21}	0.94	3.09 ^{+0.1} _{-0.1}	1.41 ^{+0.23} _{-0.22}	24.04 ^{+0.46} _{-0.45}	0.94	2.94 ^{+0.09} _{-0.09}	5.08 ^{+0.61} _{-0.47}	27.30 ^{+0.62} _{-0.63}	0.95
25000	3.03 ^{+0.06} _{-0.06}	5.09 ^{+0.19} _{-0.21}	11.24 ^{+0.15} _{-0.15}	1.03	2.94 ^{+0.08} _{-0.08}	1.72 ^{+0.2} _{-0.19}	24.74 ^{+0.38} _{-0.37}	1.04	2.82 ^{+0.06} _{-0.06}	4.54 ^{+0.34} _{-0.28}	27.59 ^{+0.5} _{-0.51}	1.04
35000	3.22 ^{+0.06} _{-0.06}	4.42 ^{+0.15} _{-0.15}	10.45 ^{+0.15} _{-0.15}	1.10	3.17 ^{+0.07} _{-0.07}	1 ^{+0.16} _{-0.15}	23.01 ^{+0.34} _{-0.33}	1.11	3.05 ^{+0.07} _{-0.07}	6.55 ^{+0.86} _{-0.65}	25.86 ^{+0.5} _{-0.5}	1.12
45000	3.22 ^{+0.09} _{-0.09}	4.42 ^{+0.18} _{-0.19}	10.14 ^{+0.21} _{-0.21}	1.04	3.17 ^{+0.11} _{-0.1}	1.01 ^{+0.21} _{-0.2}	22.31 ^{+0.43} _{-0.43}	1.03	3.06 ^{+0.1} _{-0.1}	6.59 ^{+1.21} _{-0.84}	25.07 ^{+0.63} _{-0.62}	1.06
55000	3.38 ^{+0.09} _{-0.09}	4.56 ^{+0.19} _{-0.20}	9.20 ^{+0.21} _{-0.21}	1.16	3.3 ^{+0.11} _{-0.1}	1.05 ^{+0.22} _{-0.2}	21.16 ^{+0.42} _{-0.42}	1.13	3.2 ^{+0.1} _{-0.11}	6.86 ^{+1.36} _{-0.92}	23.97 ^{+0.69} _{-0.66}	1.17
65000	3.56 ^{+0.13} _{-0.12}	5.21 ^{+0.29} _{-0.32}	8.01 ^{+0.28} _{-0.28}	1.06	3.51 ^{+0.14} _{-0.14}	1.32 ^{+0.3} _{-0.28}	19.55 ^{+0.55} _{-0.54}	1.04	3.3 ^{+0.14} _{-0.15}	5.7 ^{+1.15} _{-0.78}	23.28 ^{+0.88} _{-0.82}	1.07
75000	3.20 ^{+0.18} _{-0.17}	6.26 ^{+0.48} _{-0.57}	10.06 ^{+0.42} _{-0.41}	0.95	3.02 ^{+0.24} _{-0.24}	2.46 ^{+0.5} _{-0.45}	24.08 ^{+0.81} _{-0.79}	0.93	2.88 ^{+0.16} _{-0.16}	3.83 ^{+0.5} _{-0.38}	27.64 ^{+1.23} _{-1.15}	0.96
85000	2.99 ^{+0.13} _{-0.13}	5.53 ^{+0.30} _{-0.33}	11.80 ^{+0.31} _{-0.30}	0.94	2.84 ^{+0.17} _{-0.16}	2.16 ^{+0.35} _{-0.33}	26.33 ^{+0.65} _{-0.64}	0.93	2.78 ^{+0.11} _{-0.12}	4.1 ^{+0.43} _{-0.34}	29.23 ^{+1.04} _{-0.98}	0.97
95000	3.17 ^{+0.07} _{-0.07}	5.39 ^{+0.24} _{-0.27}	11.78 ^{+0.19} _{-0.19}	0.92	3.07 ^{+0.09} _{-0.08}	1.81 ^{+0.23} _{-0.22}	27.00 ^{+0.47} _{-0.46}	0.93	2.91 ^{+0.07} _{-0.07}	4.43 ^{+0.37} _{-0.31}	30.84 ^{+0.61} _{-0.62}	0.94
105000	3.13 ^{+0.06} _{-0.06}	5.82 ^{+0.26} _{-0.29}	12.00 ^{+0.17} _{-0.17}	1.21	3.03 ^{+0.08} _{-0.08}	2.07 ^{+0.22} _{-0.21}	27.64 ^{+0.44} _{-0.43}	1.30	2.85 ^{+0.06} _{-0.06}	4.01 ^{+0.26} _{-0.22}	31.51 ^{+0.57} _{-0.58}	1.23
115000	3.16 ^{+0.09} _{-0.08}	6.32 ^{+0.36} _{-0.41}	11.81 ^{+0.23} _{-0.23}	1.05	3.04 ^{+0.11} _{-0.11}	2.43 ^{+0.3} _{-0.28}	27.97 ^{+0.56} _{-0.55}	1.04	2.85 ^{+0.08} _{-0.08}	3.75 ^{+0.28} _{-0.23}	32.07 ^{+0.77} _{-0.77}	1.06
125000	3.29 ^{+0.06} _{-0.06}	5.76 ^{+0.28} _{-0.28}	10.70 ^{+0.16} _{-0.16}	1.11	3.21 ^{+0.08} _{-0.07}	1.94 ^{+0.22} _{-0.21}	25.40 ^{+0.42} _{-0.41}	1.09	2.99 ^{+0.06} _{-0.07}	4.28 ^{+0.32} _{-0.27}	29.73 ^{+0.55} _{-0.56}	1.12
135000	3.23 ^{+0.08} _{-0.08}	5.61 ^{+0.27} _{-0.29}	10.20 ^{+0.20} _{-0.19}	0.97	3.14 ^{+0.1} _{-0.1}	1.92 ^{+0.25} _{-0.24}	23.85 ^{+0.45} _{-0.44}	0.97	2.96 ^{+0.08} _{-0.08}	4.35 ^{+0.38} _{-0.31}	27.59 ^{+0.6} _{-0.61}	0.99
145000	3.26 ^{+0.12} _{-0.12}	5.74 ^{+0.34} _{-0.39}	10.42 ^{+0.30} _{-0.29}	1.09	3.15 ^{+0.15} _{-0.14}	2.01 ^{+0.34} _{-0.32}	24.69 ^{+0.62} _{-0.60}	1.06	2.99 ^{+0.12} _{-0.12}	4.32 ^{+0.52} _{-0.4}	28.72 ^{+0.82} _{-0.84}	1.11
155000	3.37 ^{+0.13} _{-0.13}	6.17 ^{+0.38} _{-0.44}	9.87 ^{+0.32} _{-0.32}	1.09	3.25 ^{+0.15} _{-0.15}	2.18 ^{+0.36} _{-0.33}	24.30 ^{+0.63} _{-0.64}	1.08	3.02 ^{+0.12} _{-0.13}	4.06 ^{+0.45} _{-0.35}	28.90 ^{+0.86} _{-0.87}	1.10
165000	3.27 ^{+0.13} _{-0.13}	6.33 ^{+0.41} _{-0.47}	11.27 ^{+0.37} _{-0.36}	1.02	3.12 ^{+0.18} _{-0.17}	2.41 ^{+0.39} _{-0.36}	27.35 ^{+0.73} _{-0.72}	0.98	2.95 ^{+0.12} _{-0.13}	3.89 ^{+0.41} _{-0.32}	31.91 ^{+1.03} _{-1.01}	1.03
175000	3.12 ^{+0.08} _{-0.07}	5.75 ^{+0.28} _{-0.32}	12.62 ^{+0.21} _{-0.21}	1.00	2.99 ^{+0.1} _{-0.09}	2.16 ^{+0.26} _{-0.24}	29.12 ^{+0.53} _{-0.52}	0.96	2.85 ^{+0.07} _{-0.07}	4.06 ^{+0.31} _{-0.26}	33.00 ^{+0.7} _{-0.71}	1.02
185000	2.98 ^{+0.09} _{-0.08}	5.94 ^{+0.32} _{-0.37}	13.59 ^{+0.25} _{-0.24}	1.28	2.78 ^{+0.11} _{-0.11}	2.5 ^{+0.3} _{-0.29}	30.87 ^{+0.62} _{-0.60}	1.26	2.73 ^{+0.07} _{-0.08}	3.76 ^{+0.28} _{-0.23}	33.88 ^{+0.87} _{-0.85}	1.30
195000	3.02 ^{+0.06} _{-0.06}	6.35 ^{+0.30} _{-0.33}	13.77 ^{+0.18} _{-0.18}	1.20	2.88 ^{+0.08} _{-0.08}	2.59 ^{+0.24} _{-0.23}	31.75 ^{+0.50} _{-0.49}	1.23	2.74 ^{+0.05} _{-0.06}	3.61 ^{+0.19} _{-0.17}	35.29 ^{+0.67} _{-0.67}	1.22
205000	3.11 ^{+0.07} _{-0.07}	5.45 ^{+0.21} _{-0.22}	13.51 ^{+0.21} _{-0.21}	1.14	2.99 ^{+0.09} _{-0.09}	1.98 ^{+0.22} _{-0.21}	30.79 ^{+0.50} _{-0.49}	1.09	2.87 ^{+0.07} _{-0.07}	4.34 ^{+0.31} _{-0.26}	34.74 ^{+0.68} _{-0.68}	1.17
215000	3.32 ^{+0.08} _{-0.08}	4.95 ^{+0.21} _{-0.22}	11.78 ^{+0.23} _{-0.23}	1.22	3.26 ^{+0.09} _{-0.09}	1.35 ^{+0.21} _{-0.2}	27.15 ^{+0.50} _{-0.49}	1.20	3.1 ^{+0.09} _{-0.09}	5.47 ^{+0.68} _{-0.52}	31.39 ^{+0.72} _{-0.72}	1.24
225000	3.09 ^{+0.08} _{-0.08}	5.19 ^{+0.20} _{-0.22}	12.21 ^{+0.21} _{-0.20}	1.01	3 ^{+0.1} _{-0.09}	1.75 ^{+0.22} _{-0.21}	27.29 ^{+0.46} _{-0.45}	1.02	2.86 ^{+0.07} _{-0.08}	4.53 ^{+0.37} _{-0.31}	30.73 ^{+0.65} _{-0.65}	1.03
235000	3.27 ^{+0.10} _{-0.10}	5.86 ^{+0.30} _{-0.33}	10.97 ^{+0.27} _{-0.26}	1.24	3.13 ^{+0.13} _{-0.12}	2.14 ^{+0.29} _{-0.28}	26.30 ^{+0.56} _{-0.55}	1.21	2.97 ^{+0.1} _{-0.1}	4.19 ^{+0.39} _{-0.31}	30.48 ^{+0.76} _{-0.77}	1.26
245000	3.05 ^{+0.18} _{-0.17}	6.37 ^{+0.44} _{-0.52}	11.99 ^{+0.45} _{-0.44}	0.94	2.84 ^{+0.25} _{-0.23}	2.71 ^{+0.5} _{-0.45}	27.93 ^{+0.86} _{-0.84}	0.93	2.78 ^{+0.15} _{-0.16}	3.64 ^{+0.4} _{-0.31}	31.25 ^{+1.61} _{-1.43}	0.96
255000	3.02 ^{+0.14} _{-0.13}	5.52 ^{+0.28} _{-0.31}	13.25 ^{+0.37} _{-0.36}	0.93	2.88 ^{+0.18} _{-0.17}	2.12 ^{+0.34} _{-0.32}	29.72 ^{+0.73} _{-0.72}	0.91	2.82 ^{+0.12} _{-0.12}	4.2 ^{+0.45} _{-0.35}	33.20 ^{+1.16} _{-1.09}	0.96
265000	3.03 ^{+0.07} _{-0.07}	5.10 ^{+0.20} _{-0.22}	13.42 ^{+0.20} _{-0.20}	1.24	2.91 ^{+0.09} _{-0.09}	1.76 ^{+0.22} _{-0.2}	29.58 ^{+0.49} _{-0.48}	1.25	2.83 ^{+0.07} _{-0.07}	4.57 ^{+0.37} _{-0.31}	32.90 ^{+0.65} _{-0.66}	1.26
285000	3.19 ^{+0.08} _{-0.08}	5.62 ^{+0.27} _{-0.30}	12.42 ^{+0.23} _{-0.23}	1.00	3.09 ^{+0.1} _{-0.1}	1.98 ^{+0.26} _{-0.24}	28.87 ^{+0.55} _{-0.53}	0.98	2.92 ^{+0.08} _{-0.08}	4.26 ^{+0.37} _{-0.3}	33.17 ^{+0.72} _{-0.74}	1.02
295000	3.23 ^{+0.06} _{-0.06}	5.60 ^{+0.23} _{-0.25}	12.02 ^{+0.17} _{-0.17}	1.15	3.14 ^{+0.07} _{-0.07}	1.91 ^{+0.2} _{-0.19}	28.06 ^{+0.43} _{-0.42}	1.13	2.95 ^{+0.06} _{-0.06}	4.34 ^{+0.3} _{-0.26}	32.44 ^{+0.56} _{-0.57}	1.17
305000	3.04 ^{+0.07} _{-0.07}	5.72 ^{+0.23} _{-0.25}	13.42 ^{+0.19} _{-0.19}	1.16	2.87 ^{+0.09} _{-0.09}	2.3 ^{+0.23} _{-0.22}	30.57 ^{+0.48} _{-0.47}	1.08	2.79 ^{+0.06} _{-0.06}	4 ^{+0.24} _{-0.21}	33.95 ^{+0.67} _{-0.66}	1.19
315000	3.07 ^{+0.10} _{-0.10}	5.70 ^{+0.27} _{-0.29}	14.38 ^{+0.30} _{-0.30}	1.14	2.96 ^{+0.12} _{-0.12}	2.28 ^{+0.24} _{-0.23}	33.06 ^{+0.54} _{-0.54}	1.37	2.82 ^{+0.09} _{-0.09}	4.05 ^{+0.32} _{-0.27}	36.83 ^{+0.99} _{-0.96}	1.16
325000	3.05 ^{+0.09} _{-0.09}	5.83 ^{+0.25} _{-0.27}	14.65 ^{+0.29} _{-0.29}	1.16	2.86 ^{+0.13} _{-0.12}	2.4 ^{+0.27} _{-0.26}	33.63 ^{+0.63} _{-0.62}	1.11	2.8 ^{+0.08} _{-0.08}	3.95 ^{+0.27} _{-0.23}	37.44 ^{+0.99} _{-0.96}	1.19
335000	3.20 ^{+0.15} _{-0.15}	5.80 ^{+0.31} _{-0.34}	13.21 ^{+0.48} _{-0.47}	1.27	2.86 ^{+0.22} _{-0.2}	2.5 ^{+0.41} _{-0.38}	31.90 ^{+0.88} _{-0.87}	1.20	2.96 ^{+0.14} _{-0.14}	4.23 ^{+0.5} _{-0.39}	35.81 ^{+1.24} _{-1.18}	1.30
345000	3.28 ^{+0.08} _{-0.08}	5.95 ^{+0.35} _{-0.35}	12.46 ^{+0.24} _{-0.24}	0.91	3.22 ^{+0.1} _{-0.09}	2.02 ^{+0.26} _{-0.24}	29.69 ^{+0.58} _{-0.55}	0.92	2.97 ^{+0.08} _{-0.08}	4.12 ^{+0.34} _{-0.28}	34.93 ^{+0.76} _{-0.77}	0.92
355000	3.22 ^{+0.06} _{-0.06}	5.37 ^{+0.24} _{-0.26}	11.97 ^{+0.18} _{-0.18}	1.17	3.16 ^{+0.07} _{-0.07}	1.67 ^{+0.21} _{-0.2}	27.44 ^{+0.45} _{-0.44}	1.18	2.96 ^{+0.06} _{-0.07}	4.56 ^{+0.39} _{-0.32}	31.80 ^{+0.6} _{-0.61}	1.19
365000	3.18 ^{+0.08} _{-0.08}	5.34 ^{+0.25} _{-0.27}	12.95 ^{+0.23} _{-0.23}	1.04	3.08 ^{+0.1} _{-0.09}	1.78 ^{+0.24} _{-0.23}	29.63 ^{+0.55} _{-0.54}	1.01	2.94 ^{+0.08} _{-0.08}	4.55 ^{+0.43} _{-0.35}	33.87 ^{+0.72} _{-0.74}	1.06
375000	3.29 ^{+0.06} _{-0.06}	5.54 ^{+0.22} _{-0.24}	12.11 ^{+0.17} _{-0.17}	1.08	3.22 ^{+0.07} _{-0.07}	1.79 ^{+0.2} _{-0.19}	28.50 ^{+0.43} _{-0.43}	1.07	3.00 ^{+0.06} _{-0.06}	4.5 ^{+0.33} _{-0.28}	33.26 ^{+0.58} _{-0.59}	1.10

Table 10: The best fit parameter values obtained by fitting time-resolved broadband X-ray spectra of S5 observation with the snchrotron convolved BPL/LP/ $\xi - max$ models.

Time	Broken Power law					Log parabola				$\xi - max$ model		
	Γ_1	Γ_2	norm (n) ($\times 10^{-2}$)	$\frac{\chi^2}{dof}$	α	β	norm (n) ($\times 10^{-2}$)	$\frac{\chi^2}{dof}$	p	ξ_{max}	norm (n) ($\times 10^{-2}$)	$\frac{\chi^2}{dof}$
5000	3.12 ^{+0.08} _{-0.08}	4.26 ^{+0.17} _{-0.16}	13.91 ^{+0.23} _{-0.23}	0.97	2.87 ^{+0.10} _{-0.10}	1.09 ^{+0.19} _{-0.18}	29.27 ^{+0.52} _{-0.52}	0.96	2.87 ^{+0.09} _{-0.08}	6.44 ^{+0.96} _{-0.70}	31.83 ^{+0.67} _{-0.68}	0.99
15000	2.96 ^{+0.07} _{-0.07}	4.08 ^{+0.14} _{-0.13}	14.22 ^{+0.20} _{-0.20}	1.00	2.88 ^{+0.09} _{-0.09}	0.94 ^{+0.16} _{-0.15}	29.41 ^{+0.47} _{-0.46}	1.00	2.85 ^{+0.08} _{-0.07}	6.90 ^{+0.98} _{-0.72}	31.83 ^{+0.60} _{-0.61}	1.02
25000	3.12 ^{+0.15} _{-0.15}	4.49 ^{+0.22} _{-0.20}	14.61 ^{+0.46} _{-0.45}	0.97	2.98 ^{+0.19} _{-0.18}	1.19 ^{+0.29} _{-0.27}	31.78 ^{+0.86} _{-0.86}	0.93	3.00 ^{+0.16} _{-0.15}	6.44 ^{+1.50} _{-0.95}	35.20 ^{+1.07} _{-1.08}	1.01
35000	3.14 ^{+0.15} _{-0.15}	4.48 ^{+0.21} _{-0.20}	14.52 ^{+0.46} _{-0.45}	0.97	2.57 ^{+0.11} _{-0.11}	1.66 ^{+0.21} _{-0.19}	32.16 ^{+0.57} _{-0.58}	1.20	2.64 ^{+0.07} _{-0.07}	4.85 ^{+0.39} _{-0.32}	34.11 ^{+0.89} _{-0.85}	1.23
45000	2.88 ^{+0.06} _{-0.06}	4.63 ^{+0.15} _{-0.15}	14.93 ^{+0.17} _{-0.17}	1.17	2.75 ^{+0.08} _{-0.07}	1.47 ^{+0.16} _{-0.15}	31.25 ^{+0.43} _{-0.43}	1.15	2.74 ^{+0.06} _{-0.05}	5.15 ^{+0.38} _{-0.32}	33.75 ^{+0.59} _{-0.58}	1.20
55000	2.75 ^{+0.07} _{-0.07}	4.85 ^{+0.19} _{-0.18}	16.18 ^{+0.20} _{-0.20}	1.18	2.55 ^{+0.10} _{-0.10}	1.83 ^{+0.20} _{-0.19}	33.41 ^{+0.55} _{-0.55}	1.14	2.63 ^{+0.06} _{-0.06}	4.59 ^{+0.33} _{-0.27}	35.35 ^{+0.83} _{-0.81}	1.22
65000	2.77 ^{+0.05} _{-0.05}	4.65 ^{+0.15} _{-0.15}	15.87 ^{+0.15} _{-0.16}	1.11	2.62 ^{+0.07} _{-0.07}	1.58 ^{+0.16} _{-0.15}	32.58 ^{+0.43} _{-0.43}	1.12	2.65 ^{+0.05} _{-0.05}	4.88 ^{+0.31} _{-0.27}	34.61 ^{+0.59} _{-0.58}	1.15
75000	2.85 ^{+0.05} _{-0.05}	4.75 ^{+0.17} _{-0.16}	15.20 ^{+0.16} _{-0.16}	1.04	2.71 ^{+0.07} _{-0.15}	1.56 ^{+0.16} _{-0.16}	31.77 ^{+0.43} _{-0.42}	1.06	2.69 ^{+0.05} _{-0.05}	4.86 ^{+0.33} _{-0.28}	34.13 ^{+0.57} _{-0.57}	1.07
85000	2.96 ^{+0.08} _{-0.08}	5.15 ^{+0.25} _{-0.23}	14.64 ^{+0.23} _{-0.23}	0.85	2.84 ^{+0.10} _{-0.10}	1.69 ^{+0.22} _{-0.21}	31.71 ^{+0.56} _{-0.55}	0.89	2.75 ^{+0.07} _{-0.07}	4.54 ^{+0.38} _{-0.31}	34.80 ^{+0.81} _{-0.79}	0.86
95000	2.79 ^{+0.07} _{-0.07}	4.88 ^{+0.20} _{-0.19}	14.98 ^{+0.19} _{-0.19}	1.10	2.66 ^{+0.10} _{-0.10}	1.68 ^{+0.20} _{-0.19}	31.10 ^{+0.50} _{-0.50}	1.12	2.65 ^{+0.06} _{-0.06}	4.62 ^{+0.34} _{-0.29}	33.25 ^{+0.75} _{-0.73}	1.13
105000	3.02 ^{+0.13} _{-0.12}	4.45 ^{+0.19} _{-0.18}	13.84 ^{+0.35} _{-0.34}	0.88	2.87 ^{+0.16} _{-0.15}	1.26 ^{+0.25} _{-0.23}	29.59 ^{+0.71} _{-0.70}	0.86	2.88 ^{+0.12} _{-0.12}	5.95 ^{+0.69} _{-0.69}	32.40 ^{+0.94} _{-0.91}	0.89
115000	3.11 ^{+0.10} _{-0.10}	4.47 ^{+0.18} _{-0.17}	13.36 ^{+0.28} _{-0.28}	1.36	2.98 ^{+0.12} _{-0.12}	1.19 ^{+0.21} _{-0.20}	29.10 ^{+0.58} _{-0.57}	1.33	2.97 ^{+0.10} _{-0.10}	6.33 ^{+1.00} _{-0.72}	32.10 ^{+0.74} _{-0.75}	1.39
125000	3.08 ^{+0.10} _{-0.10}	4.83 ^{+0.24} _{-0.22}	13.22 ^{+0.27} _{-0.27}	1.02	2.93 ^{+0.13} _{-0.12}	1.48 ^{+0.24} _{-0.23}	29.06 ^{+0.59} _{-0.58}	0.98	2.89 ^{+0.09} _{-0.09}	5.30 ^{+0.67} _{-0.51}	32.23 ^{+0.79} _{-0.80}	1.04
135000	3.03 ^{+0.06} _{-0.06}	4.51 ^{+0.16} _{-0.15}	13.42 ^{+0.16} _{-0.16}	1.03	2.94 ^{+0.07} _{-0.07}	1.20 ^{+0.15} _{-0.15}	28.68 ^{+0.40} _{-0.39}	1.02	2.88 ^{+0.06} _{-0.06}	5.82 ^{+0.56} _{-0.45}	31.59 ^{+0.52} _{-0.52}	1.06
145000	2.99 ^{+0.06} _{-0.05}	4.30 ^{+0.14} _{-0.13}	13.76 ^{+0.15} _{-0.15}	1.24	2.91 ^{+0.07} _{-0.07}	1.07 ^{+0.14} _{-0.14}	28.86 ^{+0.38} _{-0.37}	1.23	2.86 ^{+0.06} _{-0.05}	6.23 ^{+0.63} _{-0.50}	31.53 ^{+0.39} _{-0.50}	1.27
155000	2.96 ^{+0.07} _{-0.07}	4.16 ^{+0.15} _{-0.14}	14.60 ^{+0.20} _{-0.20}	1.08	2.88 ^{+0.09} _{-0.08}	0.99 ^{+0.17} _{-0.16}	30.29 ^{+0.48} _{-0.47}	1.08	2.84 ^{+0.07} _{-0.07}	6.57 ^{+0.88} _{-0.66}	32.88 ^{+0.62} _{-0.63}	1.10
165000	3.01 ^{+0.05} _{-0.05}	4.27 ^{+0.14} _{-0.14}	14.39 ^{+0.16} _{-0.15}	1.11	2.94 ^{+0.06} _{-0.06}	1.01 ^{+0.14} _{-0.14}	30.18 ^{+0.39} _{-0.39}	1.12	2.87 ^{+0.06} _{-0.05}	6.41 ^{+0.69} _{-0.54}	33.01 ^{+0.52} _{-0.52}	1.13
175000	2.97 ^{+0.06} _{-0.06}	4.38 ^{+0.16} _{-0.15}	15.76 ^{+0.18} _{-0.18}	1.08	2.88 ^{+0.07} _{-0.07}	1.16 ^{+0.16} _{-0.15}	33.11 ^{+0.47} _{-0.46}	1.08	2.83 ^{+0.06} _{-0.06}	5.94 ^{+0.60} _{-0.48}	36.13 ^{+0.61} _{-0.61}	1.11
185000	3.04 ^{+0.10} _{-0.10}	4.58 ^{+0.19} _{-0.17}	16.05 ^{+0.32} _{-0.31}	1.02	2.92 ^{+0.12} _{-0.12}	1.30 ^{+0.22} _{-0.20}	34.61 ^{+0.67} _{-0.67}	0.99	2.89 ^{+0.10} _{-0.09}	5.72 ^{+0.74} _{-0.56}	38.16 ^{+0.90} _{-0.90}	1.04
195000	3.08 ^{+0.14} _{-0.14}	4.25 ^{+0.18} _{-0.17}	16.00 ^{+0.46} _{-0.45}	1.42	2.89 ^{+0.18} _{-0.17}	1.11 ^{+0.27} _{-0.25}	34.35 ^{+0.91} _{-0.91}	1.38	2.96 ^{+0.15} _{-0.14}	6.91 ^{+1.67} _{-1.05}	37.57 ^{+1.10} _{-1.10}	1.46
205000	2.73 ^{+0.09} _{-0.09}	4.38 ^{+0.15} _{-0.14}	18.54 ^{+0.28} _{-0.27}	1.25	2.58 ^{+0.12} _{-0.11}	1.43 ^{+0.19} _{-0.18}	37.32 ^{+0.70} _{-0.71}	1.25	2.64 ^{+0.08} _{-0.07}	5.27 ^{+0.49} _{-0.39}	39.57 ^{+1.08} _{-1.02}	1.30
215000	2.88 ^{+0.06} _{-0.06}	4.67 ^{+0.15} _{-0.14}	17.62 ^{+0.19} _{-0.19}	1.22	2.71 ^{+0.08} _{-0.07}	1.56 ^{+0.16} _{-0.16}	37.07 ^{+0.51} _{-0.50}	1.17	2.73 ^{+0.05} _{-0.05}	5.09 ^{+0.35} _{-0.30}	39.92 ^{+0.69} _{-0.69}	1.27
225000	2.87 ^{+0.07} _{-0.07}	4.68 ^{+0.16} _{-0.15}	18.63 ^{+0.23} _{-0.23}	1.14	2.74 ^{+0.09} _{-0.08}	1.51 ^{+0.17} _{-0.17}	39.06 ^{+0.58} _{-0.58}	1.15	2.73 ^{+0.06} _{-0.06}	5.07 ^{+0.39} _{-0.33}	42.17 ^{+0.82} _{-0.81}	1.18
235000	2.88 ^{+0.05} _{-0.05}	4.60 ^{+0.14} _{-0.14}	19.06 ^{+0.18} _{-0.18}	1.17	2.74 ^{+0.06} _{-0.06}	1.45 ^{+0.14} _{-0.14}	39.85 ^{+0.49} _{-0.48}	1.16	2.74 ^{+0.05} _{-0.05}	5.22 ^{+0.35} _{-0.29}	42.94 ^{+0.64} _{-0.64}	1.21
245000	2.77 ^{+0.06} _{-0.05}	4.47 ^{+0.14} _{-0.13}	20.27 ^{+0.20} _{-0.20}	1.08	2.63 ^{+0.06} _{-0.06}	1.65 ^{+0.11} _{-0.10}	42.15 ^{+0.38} _{-0.38}	1.73	2.66 ^{+0.05} _{-0.05}	5.17 ^{+0.35} _{-0.30}	43.80 ^{+0.75} _{-0.74}	1.12
255000	2.86 ^{+0.06} _{-0.06}	4.37 ^{+0.14} _{-0.14}	20.04 ^{+0.21} _{-0.21}	1.06	2.76 ^{+0.07} _{-0.07}	1.24 ^{+0.15} _{-0.15}	41.23 ^{+0.56} _{-0.55}	1.07	2.74 ^{+0.05} _{-0.05}	5.61 ^{+0.48} _{-0.39}	44.41 ^{+0.73} _{-0.73}	1.09
265000	2.76 ^{+0.06} _{-0.06}	4.26 ^{+0.14} _{-0.13}	20.30 ^{+0.21} _{-0.21}	0.98	2.64 ^{+0.07} _{-0.07}	1.26 ^{+0.15} _{-0.15}	40.79 ^{+0.56} _{-0.56}	0.99	2.66 ^{+0.05} _{-0.05}	5.54 ^{+0.45} _{-0.37}	43.32 ^{+0.75} _{-0.74}	1.01
275000	2.86 ^{+0.10} _{-0.10}	3.79 ^{+0.13} _{-0.12}	19.01 ^{+0.32} _{-0.32}	0.91	2.77 ^{+0.12} _{-0.11}	0.81 ^{+0.18} _{-0.17}	37.96 ^{+0.75} _{-0.76}	0.90	2.81 ^{+0.10} _{-0.09}	7.93 ^{+1.65} _{-1.09}	40.52 ^{+0.93} _{-0.91}	0.93
295000	2.82 ^{+0.10} _{-0.10}	3.90 ^{+0.14} _{-0.13}	16.52 ^{+0.29} _{-0.29}	0.99	2.73 ^{+0.13} _{-0.12}	0.91 ^{+0.19} _{-0.18}	32.98 ^{+0.68} _{-0.69}	0.99	2.77 ^{+0.10} _{-0.09}	7.12 ^{+1.32} _{-0.91}	35.24 ^{+0.89} _{-0.86}	1.02
305000	3.06 ^{+0.06} _{-0.06}	3.71 ^{+0.11} _{-0.10}	16.00 ^{+0.18} _{-0.18}	1.08	3.02 ^{+0.06} _{-0.06}	0.54 ^{+0.12} _{-0.11}	32.94 ^{+0.42} _{-0.42}	1.07	2.98 ^{+0.06} _{-0.06}	10.35 ^{+2.33} _{-1.52}	35.25 ^{+0.63} _{-0.62}	1.09
315000	3.01 ^{+0.05} _{-0.05}	3.79 ^{+0.11} _{-0.10}	16.10 ^{+0.16} _{-0.16}	0.92	2.95 ^{+0.06} _{-0.06}	0.65 ^{+0.12} _{-0.11}	33.03 ^{+0.40} _{-0.40}	0.92	2.92 ^{+0.06} _{-0.05}	8.91 ^{+1.48} _{-1.05}	35.46 ^{+0.56} _{-0.56}	0.94
325000	2.97 ^{+0.07} _{-0.07}	3.99 ^{+0.13} _{-0.13}	16.34 ^{+0.21} _{-0.21}	1.02	2.90 ^{+0.08} _{-0.08}	0.83 ^{+0.15} _{-0.14}	33.56 ^{+0.50} _{-0.50}	1.03	2.87 ^{+0.07} _{-0.07}	7.35 ^{+1.11} _{-0.81}	36.29 ^{+0.65} _{-0.66}	1.04
335000	3.12 ^{+0.05} _{-0.05}	4.19 ^{+0.13} _{-0.13}	15.38 ^{+0.17} _{-0.17}	0.85	3.06 ^{+0.06} _{-0.06}	0.87 ^{+0.13} _{-0.13}	32.87 ^{+0.41} _{-0.41}	0.85	2.97 ^{+0.06} _{-0.06}	7.19 ^{+0.90} _{-0.69}	36.16 ^{+0.59} _{-0.59}	0.86
345000	3.17 ^{+0.06} _{-0.05}	4.25 ^{+0.13} _{-0.14}	14.92 ^{+0.18} _{-0.18}	0.94	3.10 ^{+0.06} _{-0.06}	0.88 ^{+0.15} _{-0.14}	32.32 ^{+0.44} _{-0.44}	0.93	3.02 ^{+0.06} _{-0.06}	7.25 ^{+1.04} _{-0.77}	35.71 ^{+0.67} _{-0.65}	0.96
355000	3.24 ^{+0.09} _{-0.09}	4.23 ^{+0.18} _{-0.17}	13.88 ^{+0.28} _{-0.28}	0.93	3.20 ^{+0.11} _{-0.10}	0.77 ^{+0.19} _{-0.18}	30.22 ^{+0.57} _{-0.56}	0.92	3.10 ^{+0.11} _{-0.10}	7.83 ^{+1.81} _{-1.17}	33.65 ^{+0.86} _{-0.84}	0.94
365000	3.15 ^{+0.11} _{-0.11}	3.99 ^{+0.16} _{-0.15}	13.92 ^{+0.32} _{-0.31}	1.15	3.09 ^{+0.13} _{-0.12}	0.71 ^{+0.20} _{-0.19}	29.62 ^{+0.63} _{-0.62}	1.13	3.06 ^{+0.12} _{-0.12}	8.94 ^{+2.90} _{-1.64}	32.22 ^{+0.89} _{-0.86}	1.16
375000	3.07 ^{+0.11} _{-0.11}	4.20 ^{+0.16} _{-0.15}	14.20 ^{+0.35} _{-0.34}	1.01	2.91 ^{+0.15} _{-0.15}	1.05 ^{+0.23} _{-0.22}	30.16 ^{+0.70} _{-0.70}	1.01	2.94 ^{+0.13} _{-0.12}	6.98 ^{+1.48} _{-0.97}	32.93 ^{+0.86} _{-0.86}	1.06

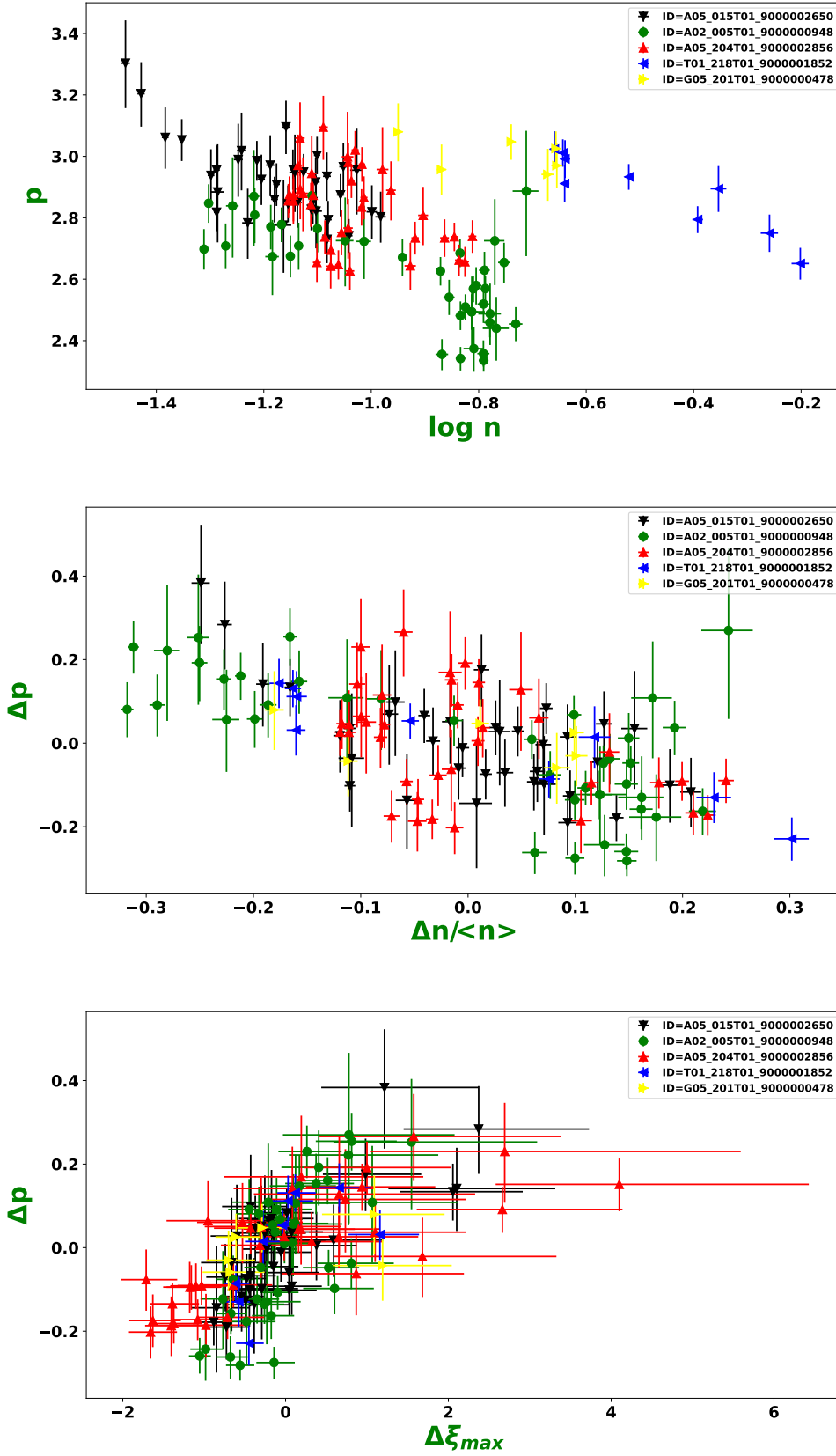


Figure 8: The correlation between the spectral parameters obtained by fitting the synchrotron convolved $\zeta - max$ model to the joint SXT and LAXPC spectrum in each time segment. Different colors in the plot depicts individual observations. The upper pannel represents relationship between p and $\log(n)$ at $\zeta = \zeta_{ref}$. The middle panel represents correlation between Δp and $\Delta n / \langle n \rangle$. The Bottom panel represents correlation between Δp and $\Delta \xi_{max}$.

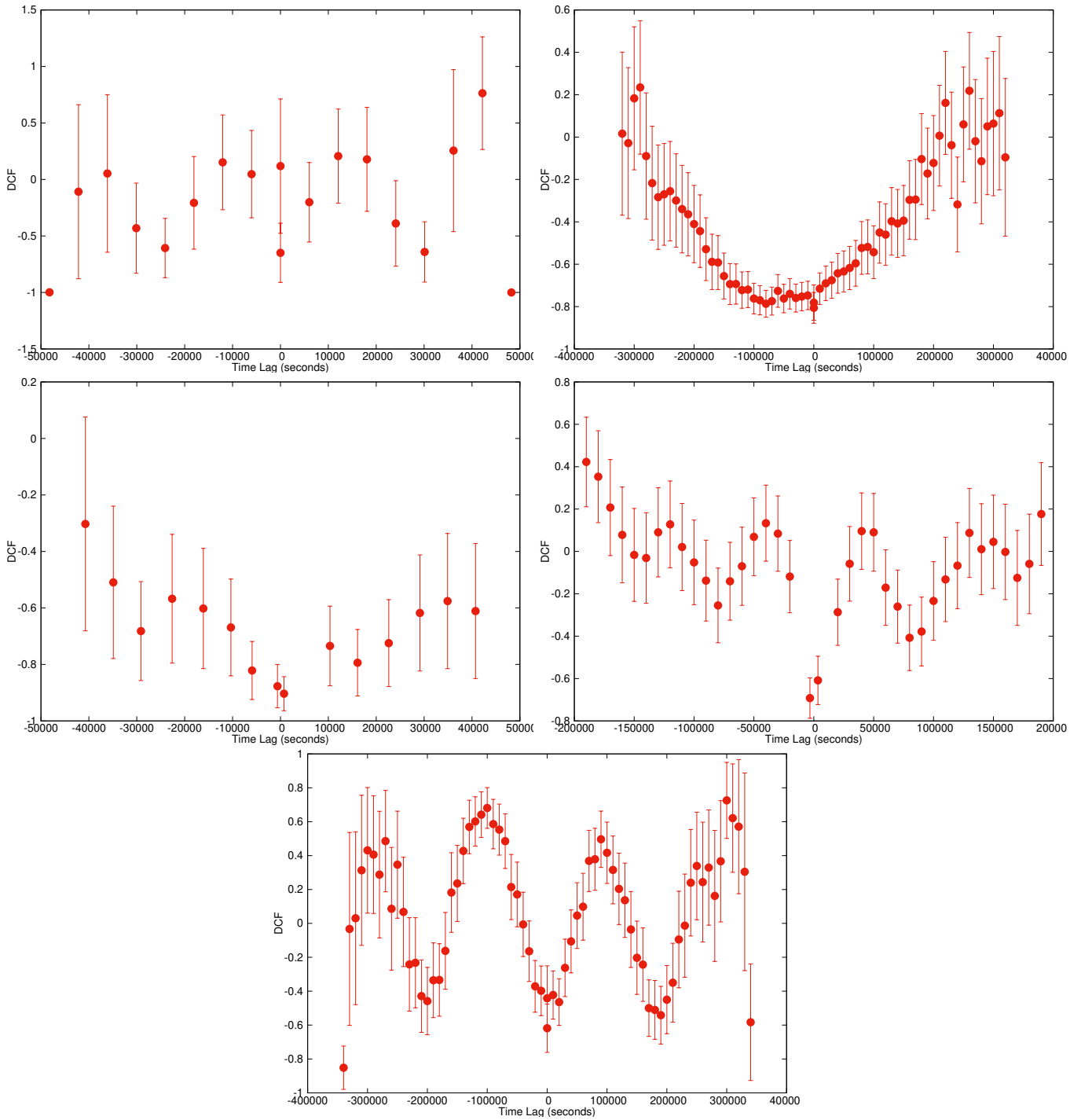


Figure 9: The discrete correlation function obtained between the variation in index and normalize particle density variation in case of BPL model. In the upper panel, DCF plots for observation S1 (left) and S2 (right) are presented. The middle panel displays DCF plots for observations S3 (left) and S4 (right). The bottom panel features the DCF plot for observation S5. The time lag is expressed in seconds.